Kinematics of the Kahramanmaraş triple junction and of Cyprus : evidence of shear partitioning

Volkan Özbey[1,2,*], Ali Mehmet Celâl Şengör[3,4], Pierre Henry[2], Mehmet Sinan Özeren[5], A. John Haines[6], Elliot C. Klein[7], Ergin Tarı[1], Cengiz Zabcı[3], Konstantinos Chousianitis[8], Sezim Ezgi Güvercin[9], Nazik Öğretmen[5]

Abstract

Triple junctions involving non-subductable plates extend beyond local implications, crucial for studying the geology of convergent plate boundary zones. However, kinematic models overlook Cyprus-Anatolia motion due to limited geodetic constraints. Our study encompasses Cyprus, southern Turkey, and the Levant coast, focusing on the Kahramanmaraş triple junction where a destructive earthquake sequence occurred on February 6, 2023. We present precise positioning data merged with published velocities, con-

*Corresponding author

Email address: ozbeyv@itu.edu.tr (Volkan Özbey)

[1]Istanbul Technical University, Department of Geomatics Engineering, 34469, Maslak, Istanbul, Turkey

[2]Aix-Marseille Universite, CNRS, IRD, INRA, Coll France, CEREGE, Aix-en-Provence, France

[3]Istanbul Technical University, Department of Geology, 34469, Maslak, Istanbul, Turkey

[4]Center for Global Tectonics, School of Earth Sciences, State Key Lab for Geological Processes and Mineral Resources, Badong National Observatory and Research Station for Geohazards, China University of Geosciences, Wuhan

[5]Istanbul Technical University, Eurasia Institute of Earth Sciences, 34469, Maslak, Istanbul, Turkey

[6]GNS Science - Institute of Geological and Nuclear Sciences, (emeritus), New Zealand

[7]FM Global Research, Research Division, Norwood, MA, United States

[8]Institute of Geodynamics, National Observatory of Athens, Lofos Nymfon, Athens, Greece

[9]Yıldız Technical University, Department of Geomatics Engineering, 34349, İstanbul, Turkey

structing an up-to-date velocity field for the interseismic period. Employing two kinematic approaches, we analyze its tectonic implications. In Cyprus, we find the relative motion of Africa (Sinai Plate) and Anatolia is partitioned between convergence in the Cyprus subduction, with rate ∼3.5-6.2 mm/yr, progressively decreasing from west to east and left-lateral transpressive Kyrenia fault, situated along the northern coast of Cyprus, with rate 3.2-4.2 mm/yr. The Levant Fault has a 3.5-4.7 mm/yr left-lateral slip rate, decreasing northward as part of it is transferred to offshore faults. The relative strike-slip motion between Arabia and Anatolia is partitioned between the East Anatolian Fault (slip rates 5.1-6.2 mm/yr) and some secondary faults such as Çardak and Malatya faults (slip rates 1.9-1.7 mm/yr) and causes distributed deformation for a 50-60 km wide region. The largest second invariant strain rate tensors from the continuum kinematic model also coincide with the same region which can be defined as the East Anatolian shear zone. A shear partitioning system exists around the Kahramanmaraş triple junction, from Cyprus to southeast Turkey. Strain rates appear relatively small in the Taurus range and Adana/Cilicia basin, transitioning from extensional/transtensional to compressional from east to west. The up component of GNSS velocities on the Taurus karstic plateau reaches 1.2 mm/yr, lower than Quaternary uplift rates on its southern edge. We examine Taurus uplift and Adana/Cilicia basin subsidence, considering slow convergence through earthquake distribution, seismic tomography, and modeling.

---

1. Introduction

The recent tectonics of the Eastern Mediterranean results from the interaction of three giant tectonic plates, Arabia, Africa and Eurasia (McKenzie et al., 1970; McKenzie, 1972; Şengör, 1979; Şengör et al., 1985). During the middle Miocene, Arabia was separated from Africa along the left-lateral Levant (or Dead Sea) fault zone (e.g., Le Pichon and Gaulier, 1988). The subsequent collision of Arabia with Europe, resulting in gravitational potential build up in Eastern Anatolia, combined with an acceleration of slab rollback in the Hellenic subduction where the northern African slab is subducted (Brun et al., 2016) and a possible contribution from underlying astenospheric flow, have been driving the westward extrusion of the Anatolian Plate (Özeren and Holt, 2010; Le Pichon and Kreemer, 2010) (Fig. 1a). At present, the boundary between Arabia and Anatolia is essentially a left lateral transform plate boundary, the East Anatolian Fault zone (EAF) (McKenzie, 1976; Şengör et al., 1985). Africa has been divided in the Eastern Mediterranean into a Nubia plate (McKenzie et al., 1970; Le Pichon and Francheteau, 1978) and a Sinai sub-plate (Mahmoud et al., 2005). This Sinai plate thus subducts beneath Anatolia along the Cyprus Arc and moves southward with respect to Arabia along the Levant Fault zone. The Kahramanmaraş triple junction is the junction of the Levant Fault zone, the East Anatolian Fault zone and the Cyprus Arc Subduction (Şengör et al., 1980, 1985; Karig and Kozlu, 1990). This triple junction gives rise to a very complex pattern of deformation in the northeastern Mediterranean because two non-subductable continental plates, namely Arabia and Anatolia, meet here. Triple junctions involving non-subductable plates have more than just local significance. It is therefore of some importance to know their characteristics for studies of the historical geology of the continental convergent plate boundary zones (Fig. 2a)(Şengör et al., 1980). During the final phases of continental collisions (Fig. 2b), the colliding continental plates often fall apart and the resulting pieces tend to move with different velocities with respect to one another (e.g., McKenzie, 1972; Roman, 1973; Dewey, 1977; Molnar and Tapponnier, 1975; Şengör, 1976; Şengör et al., 2019a). In such situations, incompatibility basins inevitably arise (Fig. 2b), as is the case in the Karlıova region in eastern Turkey (see especially Şengör, 1979; Şengör et al., 1985, 2019a), and the Adana/Cilicia region between Cyprus and Turkey (Şengör et al., 1980, 1985, 2019a). Additionally, the marine part of the Sinai Plate is formed of thinned continental crust, comprising a thicker region, the Eratosthenes

seamount (Fig. 1a), which is currently impinging the Cyprus Arc (Le Pichon et al., 2019). In this incipient collision, the relative motion of Sinai and Anatolia is distributed between the Cyprus Arc subduction, the Kyrenia fault running along the Northern Coast of Cyprus, and the Taurus range onshore further north Fig. 1b. In fact, two triple junctions are currently active in the area, namely those of Hatay (Fig. 1b) where the eastward prolongation of the Cyprus arc reaches the Levant Fault, and Kahramanmaraş where the NE prolongation of the Kyrenia fault reaches the EAF (Şengör et al., 2019a; Özkan et al., 2023). However, the motion of Cyprus with respect to Anatolia has been ignored so far in regional kinematic models because of a lack of constraints from geodesy, as there were no available data on the Island except for the single NICO station (see for example Mahmoud et al., 2005; Reilinger et al., 2006; Gomez et al., 2020).

Figure1

This paper unveils a refined GNSS (Global Navigation Satellite Systems) velocity field encompassing southern Turkey and Cyprus. Leveraging these data, we construct regional kinematic models that not only illuminate the motion of the study area but also incorporate higher-resolution boundary conditions and internal deformation characteristics specific to Cyprus. Through these novel data and models, our aim is to foster a more comprehensive understanding of the neotectonics of the northeastern Mediterranean. In addition, we will discuss the kinematic context of the major earthquakes that occurred in the Kahramanmaraş triple junction area on February 6, 2023: Mw (moment magnitude) 7.8 Pazarcık earthquake on the EAF and Mw 7.6 Elbistan earthquake on Çardak Fault (Barbot et al., 2023; Hussain et al., 2023).

Figure2

Previous geodetic studies established the plate motion and evaluated large scale internal strain of Anatolia (Reilinger et al., 2006; Özeren and Holt, 2010; Cavalié and Jónsson, 2014; England et al., 2016; Weiss et al., 2020; Bletery et al., 2020; Kurt et al., 2022) and Arabia Viltres et al. (2022) or focused on the kinematics of the Levant fault zone (Gomez et al., 2007; Le Beon et al., 2008; Alchalbi et al., 2010; Al Tarazi et al., 2011; Sadeh et al., 2012; Gomez et al., 2020; Hamiel and Piatibratova, 2021) and of the East Anatolian fault zone (Cavalié and Jónsson, 2014; Walters et al., 2014; Aktuğ et al., 2016; Bletery et al., 2020). However, only a few of them take into account the active deformation of secondary faults such as Malatya and Çardak Faults (also called Sürgü Fault by some authors) (Westaway, 2003; Aktuğ et al., 2013),

or the Karataş-Osmaniye Fault (Mahmoud et al., 2013; Özkan et al., 2023). Since vast portions of the region are situated beneath the Mediterranean Sea, observations to measure the kinematics of the Cyprus Arc Subduction are unfeasible. Cyprus, where the GNSS data have been very inadequate so far, is the only place within the Eastern Mediterranean Sea Basin where one can anchor the GNSS-based kinematic deformation models. To remedy this situation, we conducted GNSS surveys in Cyprus and revisited 18 points that have been previously measured in 1998 and 2001. We also incorporated the data from seven permanent GNSS sites in the southern part of the island. For the first time, we now have reasonable spatial coverage of space geodetic data in Cyprus enabling us to construct a kinematic model of the easternmost Mediterranean alongside a more detailed understanding of the deformation within Cyprus. Moreover, we also conducted some follow-up surveys to several GNSS survey-mode sites in the Turkish mainland to constrain the kinematics of Anatolia with better coverage. We then integrated into our velocity field previously published velocities acquired over the vicinity of the Levant fault and EAF (Gomez et al., 2020; Hamiel and Piatibratova, 2021; Kurt et al., 2022; Viltres et al., 2022). GNSS processing and integration workflow is detailed in section 2.

With the combined velocity field as input, we applied two different kinematic inversion methods. A block model is used to calculate rigid block motions and coupling on the block boundaries that are defined as dislocation sources (McCaffrey et al., 2007). The output of this model may thus be interpreted in term of long term slip rates and seismic coupling on major faults. This model also allows internal deformation of the blocks by calculating a unique and uniform strain rate tensor for each block. In parallel, we employed a continuum velocity field interpolation method to calculate the strain rate field of the study area (Haines and Holt, 1993; Beavan and Haines, 2001). This strain distribution may be compared with seismicity distribution and tectonic strain regimes indicated by fault maps.

From the modeling results, several open questions on the kinematics and tectonics of the area can be addressed. Quantifying the partitioning of deformation between the Cyprus Arc Subduction, Kyrenia fault and Taurus range is a primary outcome of the newly acquired data. Then, we evaluate the distribution of deformation around the Kahramanmaraş and Hatay triple junctions, notably between the EAF and the Karataş-Osmaniye-Çardak-Malatya fault system and discuss implications for earthquake recurrence intervals. Regarding the Levant fault, the present study is based on fewer velocity

vectors than for instance presented in Gomez et al. (2020) and has little to add to their demonstration that slip on the main fault strand is decreasing northward toward the triple junction as part of the motion is diverted offshore. Another important question is the nature of the deformation of the Adana/Cilicia basin. The basin and its frame have been interpreted as elements of a 'forearc' (e.g., Aksu et al., 2005; Fernández-Blanco, 2014; Fernández-Blanco et al., 2019, 2020; Aksu et al., 2021, and the extensive literature cited therein), but it has not been made clear how, or even whether, this alleged position has influenced its tectonic evolution. Burton-Ferguson et al. (2005) and Aksu et al. (2021) pointed out the role of the escape of the Anatolian block in inducing a strike-slip component onto the basin evolution. We will examine how the strain distribution in the basin reflects spatial and temporal changes in the boundary conditions. In the Taurus, very high Quaternary uplift rates have been reported (Cosentino et al., 2012; Schildgen et al., 2012, 2014; Cipollari et al., 2013; Radeff et al., 2017; Öğretmen et al., 2018; Racano et al., 2020) and interpreted as a consequence of slab break off or drip tectonics (Duretz and Gerya, 2013; Göğüş et al., 2017). Our results do suggest that the local shortening is indeed insufficient to explain the Quaternary uplift, and we discuss the various processes that may contribute to this effect based on seismic tomography models (Biryol et al., 2011; Abgarmi et al., 2017; Portner et al., 2018; Karabulut et al., 2019; Kounoudis et al., 2020), and also drawing on a comparison with the Alpine orogen, where Quaternary uplift is also out of proportion with crustal shortening (e.g. Sternai et al., 2019).

2. GNSS Observations and Analysis

This section commences with a thorough exposition of the dataset we acquired, followed by separate treatments of time series assessments for both continuous and survey mode sites. The analysis of continuous stations is based on a well-defined approach, the essence of which we aim to summarize in the main text. However, for a comprehensive understanding of the methodology, we encourage readers to refer to our supplementary document (sections S1-S5). All relevant sections are addressed in the corresponding part of the main text. Concluding this chapter, we integrate our initial velocity field with previously published velocities, resulting in a densified and unified velocity field.

2.1. GNSS Data

We present a GNSS velocity field that unites newly derived with previously published velocities. The raw data of the continuous stations were obtained from both international networks (International GNSS Service -IGS hereafter) and regional networks (Turkey Continuous GNSS Network and Cyprus Positioning System) (Fig. 1b). We primarily analyzed the dataset from 2009 to 2021 for continuous stations, although some of them had data gaps during that period. However, we have approximately 10 years of time series for almost every continuous site. The survey mode GNSS sites were selected from the Turkey Fundamental GNSS Network to utilize valuable existing observations and data resources. Each observation was carried out using dual-frequency receivers and a filtering cut-off angle of 10 degrees to minimize atmospheric noise. Each survey mode site has at least 7 different sessions, except for 3 sites in the northern part of Cyprus that were set up in 2019, and all sessions have at least 8 hours of observations. The readers can find further detail of the data span of survey mode sites in the supplementary file. In total, we evaluated the raw data of 137 GNSS stations (65 continuous - 72 survey mode) and estimated their velocities.

2.2. Data Evaluation

We performed data assessment using a combination of GAMIT/GLOBK software (Herring et al., 2018, and the extensive literature cited therein) and a stochastic approach. GAMIT/GLOBK integrates the double differences method and carrier phase combinations to eliminate geometric and non-dispersive delays in the solution. We used IGS final orbit and clock products as orbit parameters and the VMF1 (Vienna Mapping Function 1) mapping function to minimize the effect of the tropospheric delay (Boehm et al., 2006). In addition, we incorporated over 20 IGS stations into our network to define a well-constrained global network. We processed daily data from 2009 to 2022, while for the period between 1998 and 2009, we only evaluated days with observations for our survey-mode sites. We verified our daily solutions by following the steps outlined in Herring et al. (2018). Once the daily evaluation was successfully performed, we analyzed the time series by treating the survey mode and continuous sites differently.

2.2.1. Continuous GNSS time series

We analyzed continuous GNSS sites, characterized by uniform secular velocities and superimposed seasonal signatures. These signals are effectively

modeled using linear terms combined with sinusoids of yearly and half-yearly periods. The presence of higher-order harmonics contributing to the seasonal signals is indicated by their asymmetric behavior. To address outlying observations, we adopted a regression approach that incorporates the squares of misfits in the predictions and variances. Full details of our approach are provided in Supplementary Sections S1 and S3. Our starting point was Equ. 5 of Bevis and Brown (2014) and, like Serpelloni et al. (2022), we consider only the first two seasonal terms. Other studies raise points we address in section S1 (Johnson and Agnew, 1995; Mao et al., 1999; Bos et al., 2008). A meticulous analysis of the residuals, obtained after removing the fitted seasonal contributions, reveals specific sites exhibiting apparent changes in velocity that require special attention. Additionally, a subset of sites presents potential issues due to significant outliers from the regression model, short-duration periods of poor-quality data, or prolonged data gaps. Both horizontal and radial components are considered, with a particular focus on sites where noticeable velocity changes occur. Residuals at all sites are shown in Figures S2.1-S2.50 in Supplementary Section S2. These observations align with the findings of previous studies, providing further support and validation to the investigation (Johnson and Agnew, 1995; Mao et al., 1999; Bevis and Brown, 2014). Our analysis basically adopts a method considering correlated and dependent GNSS residuals with time following from Johnson and Agnew (1995) and Mao et al. (1999). In a more rigorous way, Bos et al. (2008) utilized spectral indices less than 1 and greater than -1. Spectral indices are dimensionless exponents in power laws relating spectral amplitudes of residuals to the inverse of frequency, and positive and negative values correspond to having dominantly low frequencies and dominantly high frequencies respectively. Based on our observations, we employ a simplified approach that attributes residual correlation primarily to seasonal variations. Though numerous other factors contribute to correlations, our spectral analysis mentioned below (see also Supplementary Sections S1 and S3-S5) confirms that this rough approximation is a good starting point. By assuming that each continuous GNSS time series comprises only two statistically independent observations per year (simplistically viewed as being independently hotter or colder than average summers and winters, or possibly wetter or dryer than average springs and autumns), we applied a correction factor to the velocity variances, resulting in larger velocity standard errors. This correction aligns with the range of values reported in previous studies.

In our study, Monte Carlo trials were conducted using 100,000 randomly

selected subsets of observations at each site (see S1.2). The subsets had a minimum interval of 6 months between observations and provided insights into velocity standard errors. Spectral analysis complemented this analysis. Velocity estimates were obtained from the subsets in the Monte Carlo trials through straight-line regressions, and despite worse misfits at bad sites, velocity standard deviations align with initial estimates. Good sites displayed normal-like statistical distributions of velocities, while bad sites did not. Irregular sampling, due to the national lockdown in the course of the COVID pandemic, posed a challenge for Fourier analysis of records at continuous mode sites. To address this, a solution involving linear interpolation between sampling times was utilized. The optimization process yielded eigenfunctions that closely resembled conventional Fourier terms when regular sampling was present. Statistical convenience favored orthogonal expansions in terms of sums over sampling times rather than integrals over time. Modifications were made to the eigenfunctions for irregular sampling to enforce orthogonality in the sum-over-sampling-times sense. Spectral analysis revealed that high-frequency spectra exhibited white noise characteristics, while low-frequency spectra displayed increased amplitudes, particularly at bad sites with apparent velocity changes.

The spectral behavior at low frequency was analyzed further (section S1.3), indicating peaks around 1 cycle/year in residuals without seasonal terms removed and a steady increase in spectral values toward lower frequencies in the case of full residuals. Low frequency behavior is consistent with finite spectral amplitudes at zero frequency. Time domain correlation functions with that property include Gaussian and exponentially decaying variance functions in the spectral domain. Gaussian and exponentially decaying variances were combined with white noise to match observed spectra. Spectral indices greater than zero were avoided due to their implications of significant correlation between observations extending to infinite time due to infinite spectral variances at zero frequency. Variances of secular velocity were estimated for components that could be fitted in this manner, while a conservative, simplified approach was taken for other components, which were the bad ones with apparent changes in velocity (section S1.4). The agreement between estimates for good components and our estimates from regression and the Monte Carlo trials was found to be satisfactory, with horizontal components showing particularly good results (see figures in the section S1.4).

The maximum of all the velocity variance estimates for each component

at each site was taken as the final standard error. The further mathematical background of the approach and additional plots pertaining to spectra of the residuals can be found in the supplementary document (sections S3, S4 and S5 respectively).

2.2.2. Survey Mode GNSS time series

The raw position time series of survey mode sites has been assessed with two main steps. We adopted a first-order Gauss Markov Extrapolation (Herring et al., 2018), embedded into GAMIT/GLOBK software, whereby we generated the velocities and their raw sigma values for each survey mode site. Once we obtained those, in the second step we followed another route to obtain more realistic standard errors by appropriately scaling them. The scaling was carried out by anchoring the campaign sites to the continuous network by using a block model inversion that involves very small blocks. At that point we would like to refer that this block model does not aim to approach any tectonic problem but rather invert for the poles of rotations for small collections of GNSS sites sufficiently close to each other so that they are almost guaranteed to obey the same rotation. The aim here is to do a grid search (Press et al., 2007) for a scaling factor for the errors of the campaign sites by keeping the errors of the continuous sites constant. The result indicates a necessary increase of errors by a factor of 2.2. A quite similar approach was adopted by Beavan et al. (2016) and they documented a very similar error scaling factor as well.

The supplementary document provides access to the NEU (North-East-Up) components of the processed station velocities and their data span (see Table S1, S2, S3).

2.3. Unifying Velocity Fields

After generating an initial velocity field, we combined it with published velocities from previous studies to obtain a GNSS field with higher density (Gomez et al., 2020; Hamiel and Piatibratova, 2021; Viltres et al., 2022; Kurt et al., 2022). To minimize the effect of the some well-known noises such as different data evaluation strategies, pre-defined reference frames from different studies etc., we rotated all these velocity fields individually with respect to our dataset.

The rotation is based on a least-square approach that aims to optimize the transformation matrix of common stations for each velocity field pair.

Table 1: Root Mean Square fit of the velocity combination. The first column includes name of the studies and second column indicates the initial reference frame of each velocity field. The third column shows the number of common station pairs.

Study	Reference Frame	N. of Common Stations	RMS (mm/yr)
Gomez et al. (2020)	ITRF08	20	0.96
Hamiel and Piatibratova (2021)	ITRF14	27	0.46
Kurt et al. (2022)	EURA_I14	65	0.57
Viltres et al. (2022)	ARAB_I14	13	0.22

Though this approach has been applied by several studies to combine velocities coming from different evaluations, we made some critical changes to the weight matrix of the objective function (see Özbey et al., 2021, eq. 4). We define a new weight parameter r_i to re-weight the covariance matrix C by $C_i r_i^{-1}$. r_i^{-1} has been constructed as the function of both distance and number of observation. According to this;

$$r_i = \begin{cases} e^{-D_i^2/n_x * n_y}, & 1 < D_i \leqslant 5 \\ e^{-1/n_x * n_y}, & D_i \leqslant 1 \end{cases} \tag{1}$$

where D_i is the distance between ith common site pair and n_x and n_y is the number of observations for the related stations x and y. Our algorithm allows utilizing a maximum of 5 km distance to decide that two sites are co-located. It also behaves as if they are exactly the same points for pairs of stations closer than 1 km. Besides, our approach takes into account the plate boundaries during its decision-making process as well. If the related station pair is in different blocks, it directly rejects it. The second parameter is the number of epochs for each site. Here it is important to note that the number of observations of permanent sites has been postulated as 365 for a year. Each velocity field has been rotated separately by taking the velocity field obtained by this study as the reference system. The statistical outcomes of these processes are listed in Table 1. The Helmert transformation parameters of each rotation are also listed in the supplementary document (S4).

Fig. 3 shows the final velocity field leveraging in the kinematic models with respect to the Arabian plate reference frame (Altamimi et al., 2017). The unified velocities with respect to both the Arabian-fixed and ITRF reference frames can be found in the supplementary material as Table S5.

Figure3

3. Modeling

In this section, we present two different modeling approaches to reveal the present-day kinematics around the Kahramanmaraş triple junction and Cyprus. The first model solution is based on a block model and is designed to indicate block motions throughout the boundaries. We suggest a block geometry for the study area and testing this geometry with previously published models. We then estimate rotation poles for the blocks and derive fault slip rates. In the next section, we introduce a continuum kinematic model and generate a continuum velocity field to monitor the deformation of the region.

3.1. Slip Rate and Locking Distribution Along the Block Boundaries

Our first model aims to determine the kinematic behavior of the Nubia-Cyprus-Anatolia tectonic system in the context of an elastic block-based approach (McCaffrey et al., 2007). Such a block model involves an inverse problem where the unknowns are, Euler vectors for individual blocks, uniform strain rate tensor for each individual block, and coupling ratios on the fault node points. The model can in principle be constrained by GNSS velocities, geological fault slip rates and the azimuth of these rates, and earthquake focal mechanisms. It is worth noting that we here only used GNSS data.

The block geometry follows the main active fault zones (Levant fault, Cyprus Arc subduction, Kyrenia fault, East Anatolian fault), which are thought to be critical in shaping the regional tectonics (Fig. 4a). The distribution of seismicity is another key feature defining some block boundaries. Our block architecture is comparable with that in previous studies (Reilinger et al., 2006; Gomez et al., 2020) except that they considered Cyprus as part of Anatolia and did not feature the Kyrenia range as a block boundary. This is justifiable as it would not have been possible to constrain the motion of a Cyprus block with the very limited GNSS data available on the island. The Kyrenia arc continues offshore toward the Adana Basin but the Cyprus block probably does not continue further east on-shore. A concentration of mostly extensional focal mechanisms is observed along a N-S trend crossing the east of the Adana/Cilicia basin, 30 km west of the Levant fault. We assumed this trend delineates a block boundary, separating Anatolia and the Cyprus block on its western side from a zone of complex deformation along the Levant and

East Anatolian faults. As internal block deformation is taken into account in the model (approximated as a uniform strain field in each block) this deforming zone can be defined as a block. The block extends eastward along the East Anatolian fault toward Malatya. The northern boundary of the block is composed of the Çardak and Malatya faults (see Fig. 4a), which are considered active (Westaway, 2003; Sançar et al., 2019; Acarel et al., 2019). An alternate geometry requiring testing is that proposed by Özkan et al. (2023) for the triple junction where the Karataş-Osmaniye Fault (KOF) connects with the East Anatolian Fault following a NE trend, instead of bending to the north toward Çardak Fault. This alternative model is presented in the supplementary material.

Figure4

To the south of Cyprus lies on the Sinai block which is largely offshore. Its motion is crucial for the kinematics of the Cyprus Arc subduction but can only be constrained by velocities along the Levant coast and in Sinai. However, GNSS velocity fields in Levant and in Southern Sinai do not fit in the same rigid block reference frame. The Levant fragment of the Sinai block may be affected by deformation along the Levant fault while south Sinai may be affected by extension around the Gulf of Aqaba. This extension cannot be well accounted for in our model, which simplifies the prolongation of the Levant fault into the Gulf of Aqaba as a vertical fault, and the subduction motion along the northern edge of the block should be better constrained by the northern stations. We thus removed all GNSS rates south of 30°N for the south Sinai. Moreover, previous studies of the Levant Fault kinematics proposed that the NE part of the Sinai microplate is fragmented in order to account for geodetic slip rates decreasing northward on the Levant fault (Gomez et al., 2020). We thus consider an additional block, referred to as the "Latakia" block, extending along the Levant coast (dashed blue line in Fig. 4a) north of Israel and compare solutions with and without this additional block. Note that Gomez et al. (2020) considers several blocks west of the Levant Fault, hence our Latakia block should be considered, like the Malatya block as a deforming block.

Along the block boundaries, we defined 5 main dislocation sources, capable of accumulating elastic deformation, on which the coupling ratio will be calculated by inversion (Fig. 4a). The Levant and East Anatolian faults, which obey nearly pure strike-slip motion, are modeled as vertical planar sources. The boundary between Anatolia and Malatya block is also simplified as a vertical fault. However, to generate the geometry of dipping faults,

such as the Cyprus subduction and Kyrenia fault, we followed published interpretations of seismic profiles (Aksu et al., 2005, 2021; Burton-Ferguson et al., 2005; Aksu et al., 2014a; Calon et al., 2005; Hall et al., 2005; Welford et al., 2015; Feld et al., 2017). We utilized, moreover, the seismicity of the region, compiling the earthquakes greater than Mw = 2.8. The earthquake locations validate the geometry of the main subduction seismogenic zone between Sinai and Cyprus down to 40 km but do not help define the geometry at depth of Kyrenia fault between Cyprus and Anatolia (Fig. 4b).

We conducted a series of synthetic tests to determine the optimal spatial resolution of node points for the slip rate distribution, which was determined by the spatial coverage of the GNSS data along both strike and dip directions. To achieve this, we utilized a checkerboard test, in which we divided the main thrust interface south of Cyprus into planar cells, and monitored the level of recovery of the given slip rate boundary conditions using synthetic GNSS velocities at the same geographic locations as our data. We tested two different average cell sizes for the thrust interface: one with an average cell size of 35 km^2, and the other with an average cell size of 10 km^2. The tests were carried out without any synthetic observation noises. Our results indicated that the test conducted with larger patches had fairly better misfits than the one consisting of finer patch resolution. Fig. S1 in the supplementary displays the checkerboard test solutions.

We test inversion results for four different block geometries based on previous publications and compared misfits obtained with these different block models. (Gomez et al., 2020; Özkan et al., 2023). In Model 1, we used the geometry published in Özkan et al. (2023) for south of Anatolia. This model has no Malatya block (see Fig.4a) between Anatolia and the EAF. For the boundary between Cyprus and Anatolia, the Karataş-Osmaniye fault (see Fig.5a) is prolonged to connect to the EAF. Model 2 is based on Model 1 with a Latakia block added. Model 3 is the block geometry depicted in Fig. 4a without the Latakia block. Model 4 is the six block geometry depicted in Fig. 4a. The solutions for models 3 and 4 have much lower misfits than the first two models, in particular in the southeastern part of the Anatolia block (see Figs. S2 and 5). Moreover, defining the eastern boundary of Cyprus block as illustrated in Fig. 4a notably reduces misfits for the stations in Cyprus. Model 4 has slightly lower misfit than Model 3, but with no reduction of the chi-2 over degree of freedom ratio (Fig.5b). An F-test, which is a powerful statistical method that allows us to assess whether the variability of the variances is significantly different, indicates this improvement is not

Table 2: Results of inversions for different block models. ${\chi_v}^2$ is the reduced chi-square (χ^2 divided by number of Degrees of Freedom (DOF)).

Model Number	DOF	χ^2	χ_v^2
1	666	4515.48	6.78
2	654	4388.34	6.71
3	632	1813.84	2.87
4	620	1791.80	2.89

significant (Table 2). This does not argue against distribution of strain west of the Levant fault as proposed by Gomez et al. (2020), but indicates that modeling this as a single added block is probably an oversimplification.

Figure5

Determining robust Euler pole parameters is of utmost importance for addressing the horizontal motion of the region. This problem is complicated by the fact that a large part of the Sinai plate is underwater and that the prolongation of the Sinai plate along the Levant coast (where GNSS stations are located) may be deforming. Euler poles of Sinai relative to Anatolia and to Arabia were obtained by the block model inversion. In order to estimate the Euler pole of the Nubia plate with respect to Anatolia we combined our determination of the Arabia-Anatolia pole with a Nubia-Arabia pole calculated in the ITRF No Net Rotation reference frame by Altamimi et al. (2017). The Nubia poles from this study and Reilinger et al. (2006) are similar to each other albeit with a slight difference in the rotation rates. The location of the Euler pole of Reilinger et al. (2006) for Sinai relative to Anatolia and ours are also close to each other. The rotation rate of the Reilinger et al. (2006) pole, however, is markedly faster resulting in a slower subduction velocity in our model. The data we used to constrain the motion of the Sinai block are essentially the same as in the previous studies, but we excluded data from South Sinai (below 30°N) as these cannot be fit in the same rigid reference frame, and this explains in large part the differences. The pole we determined provides a better fit of GNSS data along the Levant coast, but a worse fit of the GNSS data in the southern part of Sinai. We believe that this pole provides a better description of the motion of the Mediterranean seafloor as it subducts beneath Cyprus (Table 3).

After Euler poles and uniform strain rate tensor are estimated for each block a series of nonlinear inversions such as grid search and simulated annealing (Press et al., 2007) has been run iteratively to solve the coupling ratio

Table 3: Euler pole parameters estimated by this study and those coming from previous studies.

Plate Pair	Lat (°)	Lon (°)	Ω (°/Myr)	Reference
SIN - AN	31.77	37.91	-0.591	this study
SIN - AN	31.99	36.01	-1.185	Reilinger et al. (2006)
CY - AN	37.61	32.73	0.717	this study
NU - AN	31.67	34.83	-1.205	Reilinger et al. (2006)
NU - AN	31.69	34.88	-1.021	this study Altamimi et al. (2017)

Abbrevations: SIN: Sinai, AN: Anatolia, NU: Nubia, CY:Cyprus

on each node point. The Green's function that coincide with the location of the GNSS stations on the surface are determined with a rigorous approach to discretize the planar fault into rectangular patches (Okada, 1992). For the parametrization of fault coupling, we express the coupling ratio as constant between the surface and depth z1 (an inversion parameter at each node) and decaying exponentially below z2 where the fault starts fully slipping, as proposed by Wang et al. (2003).

Fig. 6a represents the block motions along the boundaries defined as dislocation sources in the model. On the Levant fault, the slip rate decreases from south to north steadily. It accommodates a 4.7 mm/yr slip rate from the Gulf of Aqaba to the Dead Sea with an almost purely left lateral strike-slip regime. However, the fault orients to the Lebanese restraining bend, and although the slip rate has still a strike-slip domination with a 3.9 mm/yr rate, it also accommodates a 1.1 mm/yr compressional rate. The Cyprus arc accommodates 3.5-6.2 mm/yr convergent rates reducing progressively from west to east. The motion of the Kyrenia fault, on the other hand, is mainly the left lateral strike-slip from the northwesternmost tip to the east of the island with rates of 3.2-4.2 mm/yr. Although the slip rates along the western prolongation of the Kyrenia fault also obey a left lateral strike-slip behavior, the spatial distribution of our dataset may not be considered capable of resolving this particular region. Along the boundary between the Anatolian and Cyprus blocks on one side and the so-called Malatya block on the other side, the inversion also indicates a $\sim$1.3 mm/yr extensional motion, which is also in agreement with the predominantly extensional style of the earthquakes (see Fig. 4a). Meanwhile, there are relatively larger velocity

residuals on the left side of the boundary, roughly coinciding with Adana Basin, that may represent active deformation not properly modeled with the assumed block geometry. As the residuals we obtained are relatively small, we present the cumulative histogram of the normalized residuals in Fig. 6b. Where the block boundary changes its azimuth from N-S to E-W and along the Çardak fault behaves as an almost left lateral strike-slip behavior with a 1.9 mm/yr rate. The Malatya fault, which extends from the eastern tip of the Çardak fault towards the north, has also left-lateral strike-slip motion accounting for 1.7 mm/yr. The motion on the East Anatolian fault zone, on the other hand, decreases from 6.2 to 5.1 mm/yr from the northernmost tip of the EAF to Kahramanmaraş triple junction where it connects with the Levant fault. Some additional shear is taken up by internal deformation of the Malatya block.

Figure6

The estimated z1 value for the Levant fault is consistently around 10 km. However, the inversion result indicates a depth of approximately 15 km (following the convention of Wang et al. (2003)) for z2 in the north of the Dead Sea, while it is inverted as 20 km for the south. For the EAF, the z1 value decreases from 20 to 13 km from south to north, while z2 remains relatively constant at 25 km. The locking behavior of the Çardak fault is relatively smooth (see Fig. 7a). The inversion estimates a z1 value around 20-25 km depth, but due to the lack of GNSS data for the offshore part, the uncertainties of the coupling coefficient are directly related to the distance between the node points and Cyprus, which is the closest location with data. The coupling distribution drastically decreases towards the west of Kyrenia fault where the dataset becomes sparse (Fig. 7b-c).

Figure7

3.2. Strain rate field

In this section, we will determine a contemporary strain rate field to characterize deformation styles in the region that comprises northeast Nubia, eastern Mediterranean Sea, Levant fault, Cyprus, Adana/Cilicia basin and neighboring southern Turkey. Our aim is to shed light on its kinematics. This can be useful for future dynamical models as kinematic constraints. In this kinematic continuum model, which is based on the method described by Haines and Holt (1993); Beavan and Haines (2001), we aim to find the minimum strain rate field that best fits the GNSS velocity field for the model region by minimizing the following objective function:

$$\sum_{\text{cells}} \nu \left(\dot{\bar{\varepsilon}}^2_{\phi\phi} + 2\dot{\bar{\varepsilon}}^2_{\phi\theta} + \dot{\bar{\varepsilon}}^2_{\theta\theta} \right) S \tag{2}$$

where $\dot{\bar{\varepsilon}}_{\phi\phi}, \dot{\bar{\varepsilon}}_{\phi\theta}$, and $\dot{\bar{\varepsilon}}_{\theta\theta}$ are strain rate tensor components with respect to longitude θ and latitude ϕ for each cell, S corresponds to the surface area of the related cell. Even though there is a possibility to prescribe the ν value, which is a weighting factor associated with the rheology of the deforming material, for each cell individually, we employed a single uniform ν value for all the cells within the domain. Further details can be found in Beavan and Haines (2001), Appendix 5.

Here, we solely utilized the GNSS velocity field without imposing any plate motion boundary conditions. To achieve the objective function, we assigned a uniform ν value. Experiments were made using larger ν values in the grid cells in SW Cyprus and further offshore where seismic catalogues show the clustering of earthquakes (see Fig.4b). If these are "damage" zones, their bulk deformability might be higher than other zones. However these experiments did not significantly improve the fit to the GNSS velocities even in the near field sites in southern Cyprus.

Fig. 8 shows the second invariant of the strain rate tensor (obeying the formula $\sqrt{\dot{e}^2_{xx} + \dot{e}^2_{yy} + 2\dot{e}^2_{xy}}$ where e_{xx}, e_{xy}, and e_{yy} are the tensor components) with seismicty. The solution indicates, in general, small strain rates within Cyprus, the second invariant rarely exceeding 20 nanostrain per year. However, there is a clear spatial variability of deformation styles on the island. A transpressive strike slip regime is found along the Kyrenia range while roughly N-S compression dominates in the southern part on the island (Fig. 9a). On a larger scale, this strain partitioning within Cyprus seems to act as a diffuse transition that rotates the predominant compression from NW-SE in the Sinai block onto NE-SW in the Cilicia basin (see Fig. 8) immediately to the north of Cyprus. Between Cyprus and Turkey the shortening integrated along the principal strain axis between the coasts of Cyprus and Turkey amounts to a maximum of 0.8 mm/yr. The lack of GNSS data (Fig. 9b) probably leads us to a strain rate field much smoother than the reality in Cilicia basin but on the large scale, the solution shows a progressive transition from compression to strike-slip toward the NE, associated with a rotation of principle axes to N-S compression and E-W extension, eventually matching the dominant strain regime found onland in Adana Basin.

Figure8

A swath of higher strain rate (more than 30 nanostrain/yr) over a width of 50-60 km is found east of the Adana basin and extends NE along the northern side of the EAF, thus defining a broader East Anatolian shear zone (Fig. 8). There, principal strain directions (E-W extension and N-S compression) are consistent with left lateral strike-slip motion. The areal strain ($\dot{e}_{xx} + \dot{e}_{yy}$) is positive (see Fig. 9) except at a few locations, indicating transtensive to extensional deformation, consistent with focal mechanisms (Fig. 8). Principal strain orientations retain the same orientation over a broader area, with lower strain rates, that includes Adana basin and the mountains north of it (Aladağlar, see Fig. 9b). Areal strain indicates extension is dominant in these mountains while both mildly transpressive and transtensive styles are found in Adana basin. This may suggest that gravity is influencing strain distribution between topographic highs and basin. The westward limit of this zone of E-W extension coincides with Ecemiş Fault (see Fig. 8). This fault zone has taken up 60 km of left lateral slip since late Eocene and is under transtension since Miocene (Jaffey and Robertson, 2005; Akif Sarıkaya et al., 2015; Yıldırım et al., 2016; Umhoefer et al., 2020). West of Ecemiş fault principal strain axes rotate to NE-SW compression and NW-SE extension, respectively parallel and perpendicular to this part of the Taurus mountain range. Ecemiş fault thus appear to bound the zone of east-west extension related to Anatolian escape. Strain rates within the Taurus range west of Ecemiş fault remain small (less than 10 nanostrain/year), areal strain is dominantly positive but changes sign toward the coast in the south-western part of the range. This is the only part of Taurus where compressive strain is currently observed.

Figure9

Along the Levant fault the dominating principal strain orientations presented in Fig. 9a are consistent with left-lateral shear on the fault. The biggest problem is that there GNSS coverage from south of Turkey along the coast towards Israel in particular for the east side of the Levant fault is poor. In Israel where the GNSS coverage is very dense, but still mostly located on the western side of the Levant fault, we see some short wavelength variability of the strain rate field with the compressional axes trending largely NW-SE. The strain rates become less coherent towards the southern tip of Israel. North of Israel the zones of higher extension (positive areal strain) and compression (negative areal strain) do not match the location of the Lebanon restraining bend. This puzzling observation has been reported before (cf. fig. 8 in Gomez et al. (2020)) and was explained by transfer of the

compression on offshore faults.

Overall, zones of higher strain rate appear to roughly correlate with zone of higher seismic activity in the 0-30 km depth range corresponding to crustal seismicity (Fig. 8). The long-term seismicity catalogue between 1905 and 2019 represented on this figure, and also projected on the cross-section in Fig. 10 was compiled from Kandilli Observatory and Earthquake Research Institute's seismicity catalogue between 1905 and 2019 (KOERI, 2001; http://www.koeri.boun.edu.tr). The magnitude of completeness of the catalogue is $\sim$Mc=4. The mean horizontal location uncertainty is less than 5 km in N-S and E-W directions. The mean of the depth uncertainty is $\sim$3.5 km, varying between 2 and 8 km. We filtered the original catalogue based on the quality factors such as horizontal location uncertainty < 5 km and RMS < 0.5 s. In the East Anatolian shear zone, the distribution of seismicity exhibits a pronounced increase along the sides of the zone, coinciding with the placement of the block boundaries. It also extends westward beneath Adana Basin and north of it where lower strain rates are obtained. The seismicity within the Taurus is comparatively lower but some concentrations of earthquakes occurs in the prolongation of the Tuz Gölü Fault (Özbey et al., 2022), along Ecemiş fault and between Mersin and Bolkardağ (see Fig. 8 and Fig. 9a). This latter zone also appears as a zone of relatively high strain rate in the GNSS interpolation with positive areal strain indicating extension. However, the orientation and style of the strain tensors determined in this area lack consistency due to relatively higher residuals around the region (Fig. 9b).

4. Discussion

In this section, we discuss our solutions and make some implications regarding to our findings by comparing them with previous studies. We mention the shear partitioning between the Cyprus subduction and Kyrenia fault in the next subsection. We then refer to the effect of this partitioning system around the East Anatolian shear zone toward the Kahramanmaraş triple junction in particular and discuss the 6 February 2023 earthquake doublet. In the third subsection, we compare our solution with the previous studies around the Levant fault and discuss the prolongation of distributed deformation for the northern part of the Levant fault. We lastly discuss the present-day uplift around the Taurus orogen and Adana/Cilicia basins region by referring to the derived strain rate field of the area and vertical

GNSS velocities. Moreover, we employ some published tomographic models and geologic interpretations to depict the discussion with various aspects.

4.1. Cyprus subduction

The slip characteristic both on Cyprus arc and Kyrenia range indicates that an ongoing shear partitioning is the dominant regime for the area. The subduction is still active in spite of the incipient collision with the Eratosthenes Seamount, with near frontal convergence at a 6.0 mm/yr rate southwest of Cyprus. The locking depth (z1) extends from the surface to 20 km depth, which is consistent with Welford et al. (2015); Feld et al. (2017). We find a nearly pure left-lateral strike-slip motion on Kyrenia fault with a rate of 3.5-4.2 mm/yr, suggesting a nearly perfect shear partitioning between the subduction and Kyrenia range. Euler poles published by previous studies (Reilinger et al., 2006; Gomez et al., 2020) only predict moderate obliquity on the Cyprus subduction, about 20° south of Cyprus, which corresponds to the critical obliquity threshold for the onset shear partitioning above a subduction zone (McCaffrey, 1992). The rotation motion of Anatolia vs. Sinai and the arc shape of the subduction cause a lateral variation of obliquity so that 20° is a minimum value, but shear partitioning above a subduction should not in principle lower slip vector obliquity below 15-20° (McCaffrey, 1992). It is thus possible that forces applied on the E and W boundaries of Cyprus block play a role. The Cyprus block interacts with the Malatya block at its NE end and conditions on this boundary are extensional. It is thus possible that the forces applied in this zone near the triple junction influence the motion of the Cyprus block and particularly the amount of strike-slip taken up in Kyrenia range.

4.2. East Anatolian shear zone

In the vicinity of the triple junction the shear between Anatolia and Arabia is distributed over a zone that we defined as a block (the Malatya block). On the East Anatolian fault, we obtain 5.1-6.2 mm/yr strike-slip rates that are lower than most previous studies (Aktuğ et al., 2016; Reilinger et al., 2006). However, analyses of a high resolution velocity field obtained combining GNSS and InSAR data (Weiss et al., 2020) found a laterally varying interseismic loading rate on the EAF (Güvercin et al., 2022; Li et al., 2023). The strike-slip rate on the Malatya fault we obtain (1.7 mm/yr) is consistent with previous studies (Aktuğ et al., 2013). The strike-slip rate on the Çardak fault we obtained from the block model is 1.8 mm/yr and is comparable with

a 2 mm/yr slip rate calculated from geomorphological offsets (Westaway, 2003). In addition, the principal strain orientations between these two faults indicate left-lateral shear co-linear with shear along the East Anatolian fault zone (see Figs. 6 and 9) with an average rate of 35 nanostrain per year and a small extensional component (Fig.8). Assuming simple shear, the internal deformation of the Malatya block over an average width of 50 km amounts to about 1.7 mm/yr. The strike-slip motion between Anatolia and Arabia thus appears to be distributed between the East Anatolian fault, the faults defining the northern boundary of the Malatya block and internal deformation of the block. These three components add up to 8.5-9.7 mm/yr, which is consistent with previous estimations of Arabia/Anatolia plate motion (Reilinger et al., 2006; Aktuğ et al., 2016; Bletery et al., 2020). The block boundaries we propose differs from the geometry proposed by Özkan et al. (2023) in that they connect the Karataş-Osmaniye fault to the EAF near Kahramanmaras and thus do not allow shear partitioning east of the triple junction. Their geometry cannot account for the loading of Çardak Fault which was ruptured during the second earthquake of the Feb 6, 2023, earthquake doublet (Toda et al., 2023; Barbot et al., 2023). Our solution with a N-S transtensional boundary connecting to Çardak fault has a lower misfit and also better represents mapped active faults (Emre et al., 2018)(Figure 1b). We conclude that part of the EAF motion is partitioned from the main fault in a broader zone around the triple junction, resulting in decreased interseismic loading rates on the main strand of the EAF.

During the Feb 6, 2023 sequence ruptures occurred on both the southern and the northern boundaries of the Malatya block. The main shock (Mw 7.8) occurred on the East Anatolian and Levant faults while the large Mw 7.6 aftershock occurred on Çardak Fault, corresponding to a moment magnitude about half of that of the main shock (Toda et al., 2023; Hussain et al., 2023). However preliminary estimates of coseismic slip from finite fault models and from optical image correlation indicate that the smaller earthquake has in fact larger displacements but over a smaller rupture length (Toda et al., 2023; Barbot et al., 2023; Li et al., 2023; Melgar et al., 2023). The occurrence of these events shows that both boundaries are seismically active and present a high seismic hazard but also suggest that recurrence interval is very different on these two faults. Estimates of surface slip from Sentinel-2 image correlation are 4 m in average over a large part of the main shock rupture with a local maximum of about 7 m, and 6 m in average for the aftershock with a maximum of 8-9 m (Barbot et al., 2023; Hussain et al., 2023). Using

our interseismic backslip estimates, recurrence intervals of 750 to 1500 year are inferred for the East Anatolian Fault and from 3000 to 5000 years on the Çardak Fault. It thus appears that triggering of the Çardak Fault does not occur each time a large earthquake occurs on the East Anatolian Fault, and probably less than once every three cycle on the EAF. Moreover the Mw 7.8 earthquake is a multi-segment rupture (Barbot et al., 2023) and such events have longer recurrence interval than those estimated for characteristic earthquakes on individual segments. Estimates from single segments range from 100 years to about 900 years along the East Anatolian Fault with the longest intervals and largest maximum magnitude (Mw 7.4) in the triple junction area (Güvercin et al., 2022). It is important to note that this study took into account a westward decrease of interseismic loading rates along the EAF segments. The duration of seismic cycles involving a multi-segment rupture is even longer. Their estimation depends on complex scenarios that combine multi-segment and single segment ruptures and ranges from 700 to 2500 years (Karabulut et al., 2023). Shear partitioning in the Kahramanmaraş triple junction is thus one of the factors contributing to very long earthquake cycles on the EAF. Moreover, the earthquake hazard on secondary faults must not be ignored even though large events on these slower faults may have even longer recurrence intervals.

4.3. Levant fault zone

Block-based model inversion indicates that the Levant fault accommodates a 3.5-4.7 mm/yr slip rate, and it decreases, slightly but steadily, from south to north. This result is consistent with previous studies such as Al Tarazi et al. (2011); Sadeh et al. (2012); Gomez et al. (2020); Hamiel and Piatibratova (2021). Gomez et al. (2020) find a decreasing motion northward from 5.0 mm/yr to 2.5-3.5 mm/yr as they consider two additional block boundaries transferring part of the Levant fault motion to hypothetical offshore structures. However, the northward decrease of the slip rate of the Levant fault found by previous studies is not well explained by a single Latakia block as this block is likely deforming. The presence of the Latakia block is crucial for delineating the zone of distributed deformation in the vicinity of the triple junction. It is nevertheless likely that a significant part of the motion on the Levant Fault is transferred to faults running along the margin (see Figs. 1 and 10). These fault then connect offshore to the Cyprus Arc subduction, which in this zone mostly accommodates strike-slip motion. Our results are thus fully consistent with previous studies.

4.4. Central Taurus and Adana/Cilicia Basin

In this section we address the possible causes of the fast recent uplift rates of Taurus and their relationship with the strain distribution within the Adana/Cilicia basin and the Cyprus arc. The present day shortening within the Taurus seems unable to explain its uplift, but one should keep in mind that Taurus is part of an orogen that has been active in several phases since the closure of the Inner Tauride Ocean in Late Eocene (Şengör et al., 2019a). Understanding present day tectonics requires knowledge of crustal and mantle structure and taking into account the evolution of Taurus and Adana/Cilicia basin since the onset of Arabia/Eurasia collision in the Miocene. Fig. 10a is a geological map showing only the rocks and structures younger than the Oligocene. All blank areas on land are pre-Miocene rocks and structures. The submarine areas are also left blank. Fig. 10b shows a simplified structural N-S cross-section at 34°E across Central Anatolia and Cyprus (Şengör et al., 2019b). For the upper mantle structure, we extracted a cross-section from a new high-resolution tomographic model of the mantle beneath it (Karabulut et al., 2019). This model is calculated by utilizing 860 broadband seismic stations to provide an improved image of the upper mantle structure in the Aegean-Anatolia domain. The model mainly exhibits major discontinuities of subducting slabs from Hellenic to Cyprus subduction zones, the readers may look at further details from Karabulut et al. (2019). We here point out that the fast uplifting part of Taurus is above cold lithosphere while hot mantle is found north of the Inner Tauride structure. This assertion is also supported by other tomographic images (Biryol et al., 2011)(Portner et al., 2018) (Kounoudis et al., 2020) and by receiver functions imaging a subhorizontal positive anomaly at 70 km depth beneath Taurus that may correspond to the top of a flat Cyprus slab (Abgarmi et al., 2017).

Figure10

Several studies have investigated the uplift dynamics of the Central Taurus in the light of a multi-phased uplift scenario since the Miocene (Cosentino et al., 2012; Schildgen et al., 2012, 2014; Cipollari et al., 2013; Radeff et al., 2017; Öğretmen et al., 2018; Racano et al., 2020) involving lithospheric mantle delamination, slab roll-back and break-off, and consequent asthenospheric upwelling. These studies relied on cosmogenic exposure ages of gravels from the Göksu River terraces (Schildgen et al., 2012), micropaleontological data from the marine deposits in Mut and Adana basins (Cosentino et al., 2012; Schildgen et al., 2012; Cipollari et al., 2013; Öğretmen et al., 2018), Miocene-aged fluvial conglomerates (Radeff et al., 2017), and abandoned marine plat-

forms (Racano et al., 2020). Cipollari et al. (2013) placed the maximum age of the surface uplift to ∼8 My based on calcareous nanoplankton ages from the Mut Basin. Radeff et al. (2017) interpreted the Upper Messinian-Lower Pliocene (5.45-5.33 My) fluvial conglomerate deposits of the Adana Basin as uplift-related and resulting in ∼4 mm/yr uplift. The latest uplift-phase was later revised by Öğretmen et al. (2018) through detailed biostratigraphic age and paleodepth reconstructions from the Early-Middle Pleistocene aged marine deposits found at ∼1 km asl in the Mut Basin pointing to ∼3.2-3.4 mm/yr uplift rate since 0.46 My (Fig. 10b). Marine terraces developed after the deposition of these marine deposits yielded similar uplift rates from 3.8-3.4 mm/yr to 1.6-1.1 mm/yr for the present-day (Racano et al., 2020).

For comparison, we extracted the vertical velocities of some particular GNSS stations. Data history and monument type are the key criteria for our selection. In order to ensure data quality and avoid potential biases we only chose stations that have at least 7 years of data span and eliminated the stations settled on building roofs. Although the vertical component of GNSS velocity vectors is less reliable than horizontal components, the up velocities of chosen GNSS sites indicate an uplift for the Taurus Range, ranging from 0.30-1.20 mm/yr and 0.8 mm/yr in Northern Cyprus (Kyrenia range). The GNSS up velocities are thus slower than the geologic estimates reported above. These differences can be in part due to the temporal scale differences between the GNSS data and geological findings. They may also be related to spatial variations of uplift rates. It is possible that the highest geological uplift rates are enhanced by erosion as they are measured near rivers that incise the southern slope of the Taurus plateau at a very high rate (Racano et al., 2020). Moreover the rapid incision of the Göksu river in the Mut Basin may feed back on the uplift rates obtained by Öğretmen et al. (2018).

While the Adana/Cilicia basin may be considered as in a fore-arc position with respect to the Cyprus subduction, its position with respect to the Taurus orogen is, at least in the early stages, that of a flexural foreland basin, analogous to the Molasse basin in the Alpine orogen (Şengör et al., 2019a). In addition, the Adana Basin and the eastern extremity of the Cilicia Basin has been affected by transtensional tectonics since the inception of the Kahramanmaras triple junction (Şengör et al., 1985; Karig and Kozlu, 1990). The stretching event induced some mafic magmatism in the eastern part of the basin and along the Amanos segment of the East Anatolian Fault (Polat et al., 1997; Parlak et al., 1998; Cosca et al., 2020). Indeed, we showed that the present day strain distribution indicates different

deformation regimes: Cilicia Basin undergoes slow NNE-SSW compression while Adana Basin is deforming under left lateral shear along a NE-SW direction. However, several studies have proposed that the subsidence of both the Adana and Cilicia basins since Mid-Miocene is in large part related to flexural bending, with only limited contribution from lateral shortening of extension (Fernández-Blanco et al., 2019; Ergin and Aktar, 2018; Williams et al., 1995). Fernández-Blanco et al. (2020) further suggested a monoclinal flexural system driven by lower crustal flow could explain both Taurus uplift and Cilicia Basin subsidence. However, they state that their model does not account for the uplift rates documented by Öğretmen et al. (2018).

The continuum deformation field (Fig. 9a) obtained in and around the Taurus mountain range shows little shortening in the upper crust (less than 1 mm/yr across the western part of Cilicia Basin). Moreover, Cyprus/Anatolia motion in the block model is dominantly strike-slip. The Anatolia-Cyprus pole we calculated would predict pure strike-slip relative motion on a fault running along the coast, which nearly follows a small circle for this pole. In fact, this strike slip-motion is dominantly taken up along the Kyrenia fault but residuals of the block model suggest left lateral strike-slip motion may be taking place along the coast of Cilicia Basin in the prolongation of Kozan Fault (see Fig. 1b). This fault had been proposed to move at rates of 4 to 8 mm/yr based on sediment depocenter migration (Aksu et al., 2014b), However the rates estimated from GNSS are barely above noise level at about one mm/yr. An analogy with the Alps may here be considered regarding convergence and uplift rates. Convergence has ceased in the Western Alps and is less than 1 mm/yr along the Central Alps cross section here considered (Walpersdorf et al., 2018; Serpelloni et al., 2016). Yet, uplift rates of 1 mm/yr to 2.5 mm/yr are observed in the core of the Alps and the widely accepted view is that post-glacial rebound and erosion cannot fully explain them, suggesting an involvement of the mantle (Sternai et al., 2019). The possibility of a recent slab break-off below the Western Alps has been proposed, but is disputed (Lippitsch et al., 2003; Zhao et al., 2016). Nevertheless slab break-off is unlikely to provide a satisfactory explanation for the Central Alps where a continuous lithospheric slab is well imaged.

Let us now examine how the present day distribution of uplift in the Taurus orogen, with maximum rates in the outer part of Taurus above cold lithosphere, could be explained by mechanical models of slab break off. In some models with weak lower crustal rheology, lithosphere delamination and slab retreat open a wide astenospheric window beneath the domain being

uplifted (Duretz and Gerya, 2013; Burov et al., 2014). This is not the case for Taurus where the zone of hot mantle lies north of the ophiolitic suture and not below the zone of present day fast uplift. However, this situation may correspond to model cases involving an eduction mechanism, that is the extrusion of a slice of crustal material between a thrust and an extensional detachment (Duretz and Gerya, 2013; Duretz et al., 2011; Burov et al., 2014). In these models the eduction process is driven by the combined buoyancy of hot astenosphere and of crustal material previously shoved into the subduction. However, the velocity field we obtain is not compatible with an eduction system as this should imply active extension within or north of the uplifting domain and, likely, higher convergence between Taurus and Cyprus than our $\simeq$1mm/yr estimate. For instance, the model proposed to explain the high uplift rates in Öğretmen et al. (2018) involves a fast horizontal displacement of the educted block, in the cm/yr range (Duretz and Gerya, 2013). Nevertheless, the apparent decoupling of uplift, upper crustal strain distribution and upper mantle buoyancy implies some kind of lower crustal flow. For instance, lower crustal channel flow giving rise to localized uplift and erosion at the edge of a plateau of thickened crust may occur without involving astenospheric upwelling (Beaumont et al., 2004). On the other hand, the forearc uplift model proposed by Fernández-Blanco et al. (2020) may be insufficient to explain the uplift rates, but this model did not fully take into account that the basement of the whole Eastern Mediterranean south of Cyprus is, probably, thinned continental crust (Le Pichon et al., 2019). This domain has been stretched in an E-W direction during the opening of the Neothetis and the northern extent of this thinned continental lithosphere is unknown. Possibly, it has been underthrust as far as beneath Central Taurus where the Moho of the subducting plate has been imaged. Drawing again on the comparison with the Alps, this situation may be analogous with the underthrusting (followed by its exhumation) of the Briançonais in the Oligocene (e.g. Jolivet et al., 2003). In this context, it seems difficult to resolve the relative contributions to the Taurus uplift of crustal buoyancy and of processes involving lithospheric slabs and the astenosphere.

5. Conclusion

Acquisition of new GNSS data on Cyprus and southern Turkey brings new insight into the deformation of the region around the Kahramanmaraş triple junction. It shows that the present-day deformation of Cyprus may

be understood as a shear partitioning system between the Cyprus arc subduction and the Kyrenia fault, which appears to be a dominantly strike-slip boundary. Thus, the incipient collision with the Eratosthenes Seamount may not have yet perturbed much the kinematics of the Cyprus subduction. On the other hand, the northeast continuation of the shear partitioning system toward the Anatolia/Arabia collision zone brings further complexity to the Kahramanmaraş triple junction.

In the Anatolia-Arabia plate boundary our study demonstrates that part of the motion on the East Anatolian Fault is distributed away from the main fault in the vicinity of the triple junction, as was previously showed for the Levant fault in the Arabia-Nubia plate boundary (Gomez et al., 2020). Thus, the EAF is not the only deformation source in the East Anatolian shear zone as deformation is also distributed on secondary faults such as Çardak and Malatya faults. The earthquake sequence that occurred on February 6 2023 emphasizes the earthquake hazard presented by secondary faults in complex plate boundary zones. In the study area the kinematics of faults offshore of the Levant and Hatay coasts still need consideration. On land the slip rates calculated on the faults bounding Malatya block result in very long earthquake cycles of 750-2000 years for the part of the EAF which ruptured recently and probably 3000-5000 years for Çardak Fault. How such rare events may be taken into account in hazard assessment poses questions.

We also showed that the part of the Taurus east of the Ecemiş Fault is subject to E-W extension related to Anatolian extrusion. On the other hand the Western part of Taurus and Cilicia Basin is under mild compression related to Cyprus arc subduction. However, the high uplift rates observed in the Taurus cannot be explained by upper crustal shortening. A combination of processes, involving lower crustal flow and mantle are needed to explain this uplift.

Acknowledgements

This study was funded by Istanbul Technical University Scientific Research Projects Coordination Unit as MGA-2020-42584 ID Number research project. Moreover, it is part of the Ph.D. thesis of the corresponding author. The modeling part was carried out mostly at Centre Européen de Recherche et d'Enseignement des Géosciences de l'Environnement (CEREGE) in the scope of the TUBITAK 2214A International Research Scholarship during Ph.D. for Ph.D. candidates program with the project number 1059B142000638.

The calculation of daily coordinates of GNSS sites reported in this paper were performed at TUBITAK ULAKBIM, High Performance and Grid Computing Center (TRUBA resources).

We would like to thank the T.C. Ministry of Defence General Directorate of Mapping for their contribution during the field studies and shared previous GNSS observations measured by them. We are grateful to Ali Fahri Özten and Sebat Proje ve Mühendislik for the instrument supplying and accommodation in Cyprus. We also want to thank Fatih Taşkıran, Mert Topal, Mustafa Ozan Güldoğan and Dr. Ali İhsan Kurt for their priceless effort during the field observations.

Dr. Robert McCaffrey's remarks guided us especially establishing the block model. We also thank Xavier Le Pichon and Solène Antoine for their comments and discussions on the understanding of the recent earthquakes. We are also grateful to Dr.Timothy Kusky for his support.

References

Abgarmi, B., Delph, J.R., Ozacar, A.A., Beck, S.L., Zandt, G., Sandvol, E., Turkelli, N., Biryol, C.B., 2017. Structure of the crust and African slab beneath the central Anatolian plateau from receiver functions: New insights on isostatic compensation and slab dynamics. Geosphere 13, 1774–1787. doi:https://doi.org/10.1130/GES01509.1.

Acarel, D., Cambaz, M.D., Turhan, F., Mutlu, A.K., Polat, R., 2019. Seismotectonics of Malatya Fault, Eastern Turkey. Open Geosciences 11, 1098–1111. doi:https://doi.org/10.1515/geo-2019-0085.

Akif Sarıkaya, M., Yıldırım, C., Çiner, A., 2015. Late Quaternary alluvial fans of Emli Valley in the Ecemiş Fault Zone, south central Turkey: Insights from cosmogenic nuclides. Geomorphology 228, 512–525. doi:https://doi.org/10.1016/j.geomorph.2014.10.008.

Aksu, A., Calon, T., Hall, J., Kurtboğan, B., Gürçay, S., Çifçi, G., 2014a. Complex interactions fault fans developed in a strike-slip system: Kozan Fault Zone, Eastern Mediterranean Sea. Marine Geology 351, 91–107. doi:https://doi.org/10.1016/j.margeo.2014.03.009.

Aksu, A., Calon, T., Hall, J., Mansfield, S., Yaşar, D., 2005. The Cilicia–Adana basin complex, Eastern Mediterranean: Neogene evolution of an

active fore-arc basin in an obliquely convergent margin. Marine Geology 221, 121–159. doi:https://doi.org/10.1016/j.margeo.2005.03.011.

Aksu, A., Hall, J., Yaltırak, C., 2021. Miocene–Quaternary tectonic, kinematic and sedimentary evolution of the eastern Mediterranean Sea: A regional synthesis. Earth-Science Reviews 220, 103719. doi:https://doi.org/10.1016/j.earscirev.2021.103719.

Aksu, A., Walsh-Kennedy, S., Hall, J., Hiscott, R., Yaltırak, C., Akhun, S., Çifçi, G., 2014b. The Pliocene–Quaternary tectonic evolution of the Cilicia and Adana basins, eastern Mediterranean: Special reference to the development of the Kozan Fault zone. Tectonophysics 622, 22–43. doi:https://doi.org/10.1016/j.tecto.2014.03.025.

Aktuğ, B., Özener, H., Doğru, A., Sabuncu, A., Turgut, B., Halıcıoğlu, K., Yılmaz, O., Havazlı, E., 2016. Slip rates and seismic potential on the East Anatolian Fault System using an improved GPS velocity field. Journal of Geodynamics 94-95, 1–12. doi:https://doi.org/10.1016/j.jog.2016.01.001.

Aktuğ, B., Parmaksız, E., Kurt, M., Lenk, O., Kılıçoğlu, A., Gürdal, M.A., Özdemir, S., 2013. Deformation of Central Anatolia: GPS implications. Journal of Geodynamics 67, 78–96. doi:https://doi.org/10.1016/j.jog.2012.05.008. wEGENER 2010.

Al Tarazi, E., Abu Rajab, J., Gomez, F., Cochran, W., Jaafar, R., Ferry, M., 2011. GPS measurements of near-field deformation along the southern Dead Sea Fault System. Geochemistry, Geophysics, Geosystems 12. doi:https://doi.org/10.1029/2011GC003736.

Alchalbi, A., Daoud, M., Gomez, F., McClusky, S., Reilinger, R., Romeyeh, M.A., Alsouod, A., Yassminh, R., Ballani, B., Darawcheh, R., Sbeinati, R., Radwan, Y., Masri, R.A., Bayerly, M., Ghazzi, R.A., Barazangi, M., 2010. Crustal deformation in northwestern Arabia from GPS measurements in Syria: Slow slip rate along the northern Dead Sea Fault. Geophysical Journal International 180, 125–135. doi:https://doi.org/10.1111/j.1365-246X.2009.04431.x.

Altamimi, Z., Métivier, L., Rebischung, P., Rouby, H., Collilieux, X., 2017. ITRF2014 plate motion model. Geophysical Journal International 209, 1906–1912. doi:https://doi.org/10.1093/gji/ggx136.

Barbot, S., Luo, H., Wang, T., Hamiel, Y., Piatibratova, O., Javed, M.T., Braitenberg, C., Gurbuz, G., 2023. Slip distribution of the February 6, 2023 Mw 7.8 and Mw 7.6, Kahramanmaraş, Turkey earthquake sequence in the East Anatolian Fault Zone. Seismica 2. doi:https://seismica.library.mcgill.ca/article/view/502.

Beaumont, C., Jamieson, R.A., Nguyen, M.H., Medvedev, S., 2004. Crustal channel flows: 1. Numerical models with applications to the tectonics of the Himalayan-Tibetan orogen. Journal of Geophysical Research: Solid Earth 109. doi:https://doi.org/10.1029/2003JB002809.

Beavan, J., Haines, J., 2001. Contemporary horizontal velocity and strain rate fields of the Pacific-Australian plate boundary zone through New Zealand. Journal of Geophysical Research: Solid Earth 106, 741–770. doi:https://doi.org/10.1029/2000jb900302.

Beavan, J., Wallace, L.M., Palmer, N., Denys, P., Ellis, S., Fournier, N., Hreinsdottir, S., Pearson, C., Denham, M., 2016. New Zealand GPS velocity field: 1995–2013. New Zealand Journal of Geology and Geophysics 59, 5–14. doi:https://doi.org/10.1080/00288306.2015.1112817.

Bevis, M., Brown, A., 2014. Trajectory models and reference frames for crustal motion geodesy. Journal of Geodesy 88, 283–311. doi:https://doi.org/10.1007/s00190-013-0685-5.

Biryol, B.C., Beck, S.L., Zandt, G., Ozacar, A.A., 2011. Segmented African lithosphere beneath the Anatolian region inferred from teleseismic P-wave tomography. Geophysical Journal International 184, 1037–1057. doi:https://doi.org/10.1111/j.1365-246X.2010.04910.x.

Bletery, Q., Cavalié, O., Nocquet, J.M., Ragon, T., 2020. Distribution of Interseismic Coupling Along the North and East Anatolian Faults Inferred From InSAR and GPS Data. Geophysical Research Letters 47, e2020GL087775. doi:https://doi.org/10.1029/2020GL087775. e2020GL087775 10.1029/2020GL087775.

Boehm, J., Werl, B., Schuh, H., 2006. Troposphere mapping functions for GPS and very long baseline interferometry from European Centre for Medium-Range Weather Forecasts operational analysis data. Journal of

Geophysical Research: Solid Earth 111. doi:https://doi.org/10.1029/2005JB003629.

Bos, M., Fernandes, R., Williams, S., Bastos, L., 2008. Fast error analysis of continuous GPS observations. Journal of Geodesy 82, 157–166. doi:https://doi.org/10.1007/s00190-007-0165-x.

Brun, J.P., Faccenna, C., Gueydan, F., Sokoutis, D., Philippon, M., Kydonakis, K., Gorini, C., 2016. The two-stage Aegean extension, from localized to distributed, a result of slab rollback acceleration. Canadian Journal of Earth Sciences 53, 1142–1157. doi:https://10.1139/cjes-2015-0203.

Burov, E., Francois, T., Agard, P., Le Pourhiet, L., Meyer, B., Tirel, C., Lebedev, S., Yamato, P., Brun, J.P., 2014. Rheological and geodynamic controls on the mechanisms of subduction and HP/UHP exhumation of crustal rocks during continental collision: Insights from numerical models. Tectonophysics 631, 212–250. doi:https://doi.org/10.1016/j.tecto.2014.04.033. observational and Modelling perspectives on the Mechanical properties of the Lithosphere.

Burton-Ferguson, R., Aksu, A., Calon, T., Hall, J., 2005. Seismic stratigraphy and structural evolution of the Adana Basin, eastern Mediterranean. Marine Geology 221, 189–222. doi:https://doi.org/10.1016/j.margeo.2005.03.009.

Calon, T., Aksu, A., Hall, J., 2005. The Neogene evolution of the outer Latakia Basin and its extension into the eastern Mesaoria Basin (Cyprus), eastern Mediterranean. Marine Geology 221, 61–94. doi:https://doi.org/10.1016/j.margeo.2005.03.013.

Cavalié, O., Jónsson, S., 2014. Block-like plate movements in eastern Anatolia observed by InSAR. Geophysical Research Letters 41, 26–31. doi:https://doi.org/10.1002/2013GL058170.

Cipollari, P., Halasova, E., Guerbuez, K., Cosentino, D., 2013. Middle-Upper Miocene paleogeography of southern Turkey: insights from stratigraphy and calcareous nannofossil biochronology of the Olukpınar and Başyayla sections (Mut-Ermenek Basin). Turkish Journal of Earth Sciences 22, 820–838. doi:https://doi.org/10.3906/yer-1208-2.

Cosca, M.A., Reid, M., Delph, J.R., Kuşcu, G.G., Blichert-Toft, J., Premo, W., Whitney, D.L., Teyssier, C., Rojay, B., 2020. Age and mantle sources of Quaternary basalts associated with "leaky" transform faults of the migrating Anatolia-Arabia-Africa triple junction. Geosphere 17, 69–94. doi:10.1130/GES02266.1.

Cosentino, D., Schildgen, T.F., Cipollari, P., Faranda, C., Gliozzi, E., Hudáčková, N., Lucifora, S., Strecker, M.R., 2012. Late Miocene surface uplift of the southern margin of the Central Anatolian Plateau, Central Taurides, Turkey. Bulletin 124, 133–145. doi:https://doi.org/10.1130/B30466.1.

Dewey, J.F., 1977. Suture zone complexities: a review. Tectonophysics 40, 53–67. doi:https://doi.org/10.1016/0040-1951(77)90029-4.

Duretz, T., Gerya, T., 2013. Slab detachment during continental collision: Influence of crustal rheology and interaction with lithospheric delamination. Tectonophysics 602, 124–140. doi:https://doi.org/10.1016/j.tecto.2012.12.024. tOPO-EUROPE III.

Duretz, T., Gerya, T.V., May, D.A., 2011. Numerical modelling of spontaneous slab breakoff and subsequent topographic response. Tectonophysics 502, 244–256. doi:https://doi.org/10.1016/j.tecto.2010.05.024. tOPO-EUROPE II - From Iberia to the Carpathians and analogues.

Ekström, G., Nettles, M., 1997. Calibration of the HGLP seismograph network and centroid-moment tensor analysis of significant earthquakes of 1976. Physics of the Earth and Planetary Interiors 101, 219–243. doi:https://doi.org/10.1016/S0031-9201(97)00002-2.

Emre, Ö., Duman, T., Özalp, S., Elmacı, H., Olgun, Ş., Şaroğlu, F., 2013. Active fault map of Turkey with explanatory text. General Directorate of Mineral Research and Exploration Special Publication Series 30.

Emre, Ö., Duman, T.Y., Özalp, S., Şaroğlu, F., Olgun, Ş., Elmacı, H., Can, T., 2018. Active fault database of Turkey. Bulletin of Earthquake Engineering 16, 3229–3275.

England, P., Houseman, G., Nocquet, J.M., 2016. Constraints from GPS measurements on the dynamics of deformation in Anatolia and the Aegean.

Journal of Geophysical Research: Solid Earth 121, 8888–8916. doi:https://doi.org/10.1002/2016JB013382.

Ergin, M., Aktar, M., 2018. Lower crustal seismic activity in the Adana Basin (Eastern Mediterranean): Possible connection to gravitational flexure. Tectonophysics 730, 1–10. doi:https://doi.org/10.1016/j.tecto.2018.02.015.

Feld, C., Mechie, J., Hübscher, C., Hall, J., Nicolaides, S., Gurbuz, C., Bauer, K., Louden, K., Weber, M., 2017. Crustal structure of the Eratosthenes Seamount, Cyprus and S. Turkey from an amphibian wide-angle seismic profile. Tectonophysics 700-701, 32–59. doi:https://doi.org/10.1016/j.tecto.2017.02.003.

Fernández-Blanco, D., 2014. Evolution of Orogenic Plateaus at Subduction Zones-Sinking and raising the southern margin of the Central Anatolian Plateau. Ph.D. thesis. Vrije Universiteit Amsterdam. URL: https://thesiscommons.org/hf759/.

Fernández-Blanco, D., Bertotti, G., Aksu, A., Hall, J., 2019. Monoclinal flexure of an orogenic plateau margin during subduction, south Turkey. Basin Research 31, 709–727. doi:https://doi.org/10.1111/bre.12341.

Fernández-Blanco, D., Mannu, U., Bertotti, G., Willett, S.D., 2020. Forearc high uplift by lower crustal flow during growth of the Cyprus-Anatolian margin. Earth and Planetary Science Letters 544, 116314. doi:https://doi.org/10.1016/j.epsl.2020.116314.

Gomez, F., Cochran, W.J., Yassminh, R., Jaafar, R., Reilinger, R., Floyd, M., King, R.W., Barazangi, M., 2020. Fragmentation of the Sinai Plate indicated by spatial variation in present-day slip rate along the Dead Sea Fault System. Geophysical Journal International 221, 1913–1940. doi:https://doi.org/10.1093/gji/ggaa095.

Gomez, F., Karam, G., Khawlie, M., McClusky, S., Vernant, P., Reilinger, R., Jaafar, R., Tabet, C., Khair, K., Barazangi, M., 2007. Global Positioning System measurements of strain accumulation and slip transfer through the restraining bend along the Dead Sea fault system in Lebanon. Geophysical Journal International 168, 1021–1028. doi:https://doi.org/10.1111/j.1365-246X.2006.03328.x.

Göğüş, O.H., Pysklywec, R.N., Şengör, A.M.C., Gün, E., 2017. Drip tectonics and the enigmatic uplift of the Central Anatolian Plateau. Nature Communications 8, 1538. doi:https://doi.org/10.1038/s41467-017-01611-3.

Güvercin, S.E., Karabulut, H., Konca, A.O., Doğan, U., Ergintav, S., 2022. Active seismotectonics of the East Anatolian Fault. Geophysical Journal International 230, 50–69.

Haines, A.J., Holt, W.E., 1993. A procedure for obtaining the complete horizontal motions within zones of distributed deformation from the inversion of strain rate data. Journal of Geophysical Research 98. doi:https://doi.org/10.1029/93jb00892.

Hall, J., Calon, T., Aksu, A., Meade, S., 2005. Structural evolution of the Latakia Ridge and Cyprus Basin at the front of the Cyprus Arc, eastern Mediterranean Sea. Marine Geology 221, 261–297. doi:https://doi.org/10.1016/j.margeo.2005.03.007.

Hamiel, Y., Piatibratova, O., 2021. Spatial Variations of Slip and Creep Rates Along the Southern and Central Dead Sea Fault and the Carmel–Gilboa Fault System. Journal of Geophysical Research: Solid Earth 126, e2020JB021585. doi:https://doi.org/10.1029/2020JB021585.

Herring, T., King, R., Floyd, M., McClusky, S., 2018. Introduction to GAMIT/GLOBK, Release 10.7, GAMIT/GLOBK Documentation.

Hussain, E., Kalaycıoğlu, S., Milliner, C.W., Çakir, Z., 2023. Preconditioning the 2023 Kahramanmaraş (Türkiye) earthquake disaster. Nature Reviews Earth and Environment , 5–7doi:https://10.1038/s43017-023-00411-2.

Jaffey, N., Robertson, A., 2005. Non-marine sedimentation associated with Oligocene-Recent exhumation and uplift of the Central Taurus Mountains, S Turkey. Sedimentary Geology 173, 53–89. doi:https://doi.org/10.1016/j.sedgeo.2003.11.025. cenozoic Sedimentary Basins of South Turkey.

Johnson, H.O., Agnew, D.C., 1995. Monument motion and measurements of crustal velocities. Geophysical Research Letters 22, 2905–2908. doi:https://doi.org/10.1029/95GL02661.

Jolivet, L., Faccenna, C., Goffé, B., Burov, E., Agard, P., 2003. Subduction tectonics and exhumation of high-pressure metamorphic rocks in the Mediterranean orogens. American Journal of Science 303, 353–409. doi:https://doi.org/10.2475/ajs.303.5.353.

Karabulut, H., Güvercin, S.E., Hollingsworth, J., Konca, A.O., 2023. Long silence on the East Anatolian Fault Zone (Southern Turkey) ends with devastating double earthquakes (6 February 2023) over a seismic gap: implications for the seismic potential in the Eastern Mediterranean region. Journal of the Geological Society 180. doi:https://doi.org/10.1144/jgs2023-021.

Karabulut, H., Paul, A., Özbakır, A.D., Ergün, T., Şentürk, S., 2019. A new crustal model of the Anatolia–Aegean domain: evidence for the dominant role of isostasy in the support of the Anatolian plateau. Geophysical Journal International 218, 57–73. doi:https://doi.org/10.1093/gji/ggz147.

Karig, D.E., Kozlu, H., 1990. Late Palaeogene-Neogene evolution of the triple junction region near Maraş, south-central Turkey. Journal of the Geological Society 147, 1023–1034. doi:https://doi.org/10.1144/gsjgs.147.6.1023.

Kounoudis, R., Bastow, I.D., Ogden, C.S., Goes, S., Jenkins, J., Grant, B., Braham, C., 2020. Seismic Tomographic Imaging of the Eastern Mediterranean Mantle: Implications for Terminal-Stage Subduction, the Uplift of Anatolia, and the Development of the North Anatolian Fault. Geochemistry, Geophysics, Geosystems 21, e2020GC009009. doi:https://doi.org/10.1029/2020GC009009.

Kurt, I.A., Özbakir, D.A., Cingoz, A., Ergintav, S., Dogan, U., Özarpaci, S., 2022. Contemporary velocity field for Turkey inferred from combination of a dense network of long term GNSS observations. Turkish Journal of Earth Sciences doi:https://doi.org/10.55730/yer-2203-13.

Le Beon, M., Klinger, Y., Amrat, A.Q., Agnon, A., Dorbath, L., Baer, G., Ruegg, J.C., Charade, O., Mayyas, O., 2008. Slip rate and locking depth from GPS profiles across the southern Dead Sea Transform. Journal of Geophysical Research: Solid Earth 113. doi:https://doi.org/10.1029/2007JB005280.

Le Pichon, X., Francheteau, J., 1978. A plate-tectonic analysis of the Red Sea—Gulf of Aden Area. Tectonophysics 46, 369–406. doi:https://doi.org/10.1016/0040-1951(78)90214-7. structure and Tectonics of the Eastern Mediterranean.

Le Pichon, X., Gaulier, J.M., 1988. The rotation of Arabia and the Levant fault system. Tectonophysics 153, 271–294. doi:https://doi.org/10.1016/0040-1951(88)90020-0. the gulf of Suez and red sea rifting.

Le Pichon, X., Kreemer, C., 2010. The Miocene-to-Present Kinematic Evolution of the Eastern Mediterranean and Middle East and Its Implications for Dynamics. Annual Review of Earth and Planetary Sciences 38, 323–351. doi:https://doi.org/10.1146/annurev-earth-040809-152419.

Le Pichon, X., Şengör, A.C., İmren, C., 2019. A new approach to the opening of the eastern Mediterranean Sea and the origin of the Hellenic subduction zone. Part 2: The Hellenic subduction zone. Canadian Journal of Earth Sciences 56, 1144–1162. doi:https://doi.org/10.1139/cjes-2018-0315.

Li, S., Wang, X., Tao, T., Zhu, Y., Qu, X., Li, Z., Huang, J., Song, S., 2023. Source Model of the 2023 Turkey Earthquake Sequence Imaged by Sentinel-1 and GPS Measurements: Implications for Heterogeneous Fault Behavior along the East Anatolian Fault Zone. Remote Sensing 15. doi:10.3390/rs15102618.

Lippitsch, R., Kissling, E., Ansorge, J., 2003. Upper mantle structure beneath the Alpine orogen from high-resolution teleseismic tomography. Journal of Geophysical Research: Solid Earth 108. doi:https://doi.org/10.1029/2002JB002016.

Mahmoud, S., Reilinger, R., McClusky, S., Vernant, P., Tealeb, A., 2005. GPS evidence for northward motion of the Sinai Block: implications for E. Mediterranean tectonics. Earth and Planetary Science Letters 238, 217–224. doi:https://doi.org/10.1016/j.epsl.2005.06.063.

Mahmoud, Y., Masson, F., Meghraoui, M., Cakir, Z., Alchalbi, A., Yavasoglu, H., Yönlü, O., Daoud, M., Ergintav, S., Inan, S., 2013. Kinematic study at the junction of the East Anatolian fault and the Dead

Sea fault from GPS measurements. Journal of Geodynamics 67, 30–39. doi:https://doi.org/10.1016/j.jog.2012.05.006.

Mao, A., Harrison, C.G.A., Dixon, T.H., 1999. Noise in GPS coordinate time series. Journal of Geophysical Research: Solid Earth 104, 2797–2816. doi:https://doi.org/10.1029/1998JB900033.

McCaffrey, R., 1992. Oblique plate convergence, slip vectors, and forearc deformation. Journal of Geophysical Research: Solid Earth 97, 8905–8915. doi:https://doi.org/10.1029/92JB00483.

McCaffrey, R., Qamar, A.I., King, R.W., Wells, R., Khazaradze, G., Williams, C.A., Stevens, C.W., Vollick, J.J., Zwick, P.C., 2007. Fault locking, block rotation and crustal deformation in the Pacific Northwest. Geophysical Journal International 169, 1315–1340. doi:https://doi.org/10.1111/j.1365-246X.2007.03371.x.

McKenzie, D., 1972. Active tectonics of the Mediterranean region. Geophysical Journal International 30, 109–185. doi:https://doi.org/10.1111/j.1365-246X.1972.tb02351.x.

McKenzie, D., 1976. The East Anatolian Fault: A major structure in Eastern Turkey. Earth and Planetary Science Letters 29, 189–193. doi:https://doi.org/10.1016/0012-821X(76)90038-8.

McKenzie, D., Davies, D., Molnar, P., 1970. Plate tectonics of the Red Sea and east Africa. Nature 226, 243–248. doi:https://doi.org/10.1038/226243a0.

Melgar, D., Taymaz, T., Ganas, A., Crowell, B.W., Öcalan, T., Kahraman, M., Tsironi, V., Yolsal-Çevikbil, S., Valkaniotis, S., Irmak, T.S., et al., 2023. Sub-and super-shear ruptures during the 2023 Mw 7.8 and Mw 7.6 earthquake doublet in SE Türkiye. Seismica 2. doi:10.26443/seismica.v2i3.387.

Molnar, P., Tapponnier, P., 1975. Cenozoic Tectonics of Asia: Effects of a Continental Collision: Features of recent continental tectonics in Asia can be interpreted as results of the India-Eurasia collision. science 189, 419–426. doi:https://www.science.org/doi/10.1126/science.189.4201.419.

Öğretmen, N., Cipollari, P., Frezza, V., Faranda, C., Karanika, K., Gliozzi, E., Radeff, G., Cosentino, D., 2018. Evidence for 1.5 km of uplift of the Central Anatolian Plateau's southern margin in the last 450 kyr and implications for its multiphased uplift history. Tectonics 37, 359–390. doi:https://doi.org/10.1002/2017TC004805.

Okada, Y., 1992. Internal deformation due to shear and tensile faults in a half-space. Bulletin of the Seismological Society of America 82, 1018–1040. doi:https://doi.org/10.1785/BSSA0820021018.

Özbey, V., Özeren, M.S., Henry, P., Klein, E., Galgana, G., Karabulut, H., Lange, D., McCaffrey, R., 2021. Kinematics of the Marmara Region: a fusion of continuum and block models. Mediterranean Geoscience Reviews 3, 57–78. doi:https://doi.org/10.1007/s42990-021-00051-y.

Özbey, V., Şengör, A.M.C., Özeren, M.S., 2022. Tectonics in a very slowly deforming region in an orogenic belt. Tectonophysics 827, 229272. doi:https://doi.org/10.1016/j.tecto.2022.229272.

Özeren, M.S., Holt, W.E., 2010. The dynamics of the eastern Mediterranean and eastern Turkey. Geophysical Journal International 183, 1165–1184. doi:https://doi.org/10.1111/j.1365-246X.2010.04819.x.

Parlak, O., Kop, A., Unlugenc, U.C., Demirkol, C., 1998. Geochronology and Geochemistry of Basaltic Rocks in The Karasu Graben Around Kırıkhan (Hatay), S . Turkey. Turkish Journal of Earth Sciences 7, 53–62. doi:https://journals.tubitak.gov.tr/earth/vol7/iss2/1.

Polat, A., Kerrich, R., Casey, J., 1997. Geochemistry of Quaternary basalts erupted along the east Anatolian and Dead Sea fault zones of southern Turkey: implications for mantle sources. Lithos 40, 55–68. doi:https://doi.org/10.1016/S0024-4937(96)00027-8.

Portner, D.E., Delph, J.R., Biryol, C.B., Beck, S.L., Zandt, G., Özacar, A.A., Sandvol, E., Türkelli, N., 2018. Subduction termination through progressive slab deformation across Eastern Mediterranean subduction zones from updated P-wave tomography beneath Anatolia. Geosphere 14, 907–925. doi:https://doi.org/10.1130/GES01617.1.

Press, W.H., Teukolsky, S.A., Vetterling, W.T., Flannery, B.P., 2007. Numerical recipes 3rd edition: The art of scientific computing. Cambridge university press.

Racano, S., Jara-Muñoz, J., Cosentino, D., Melnick, D., 2020. Variable quaternary uplift along the southern margin of the central Anatolian plateau inferred from modeling marine terrace sequences. Tectonics 39, e2019TC005921. doi:https://doi.org/10.1029/2019TC005921.

Radeff, G., Schildgen, T.F., Cosentino, D., Strecker, M.R., Cipollari, P., Darbaş, G., Gürbüz, K., 2017. Sedimentary evidence for late Messinian uplift of the SE margin of the Central Anatolian Plateau: Adana Basin, southern Turkey. Basin Research 29, 488–514. doi:https://doi.org/10.1111/bre.12159.

Reilinger, R., McClusky, S., Vernant, P., Lawrence, S., Ergintav, S., Cakmak, R., Ozener, H., Kadirov, F., Guliev, I., Stepanyan, R., Nadariya, M., Hahubia, G., Mahmoud, S., Sakr, K., ArRajehi, A., Paradissis, D., Al-Aydrus, A., Prilepin, M., Guseva, T., Evren, E., Dmitrotsa, A., Filikov, S.V., Gomez, F., Al-Ghazzi, R., Karam, G., 2006. GPS constraints on continental deformation in the Africa-Arabia-Eurasia continental collision zone and implications for the dynamics of plate interactions. Journal of Geophysical Research: Solid Earth 111, 1–26. doi:https://doi.org/10.1029/2005JB004051.

Roman, C., 1973. Buffering plate: set of continental collision. New Sci. 57, 830.

Sadeh, M., Hamiel, Y., Ziv, A., Bock, Y., Fang, P., Wdowinski, S., 2012. Crustal deformation along the Dead Sea Transform and the Carmel Fault inferred from 12 years of GPS measurements. Journal of Geophysical Research: Solid Earth 117. doi:https://doi.org/10.1029/2012JB009241.

Sançar, T., Zabcı, C., Karabacak, V., Yazıcı, M., Akyüz, H.S., 2019. Geometry and Paleoseismology of the Malatya Fault (Malatya-Ovacık Fault Zone), Eastern Turkey: Implications for intraplate deformation of the Anatolian Scholle. Journal of Seismology 23, 319–340. doi:https://doi.org/10.1007/s10950-018-9808-z.

Schildgen, T.F., Cosentino, D., Bookhagen, B., Niedermann, S., Yıldırım, C., Echtler, H., Wittmann, H., Strecker, M.R., 2012. Multi-phased uplift of the southern margin of the Central Anatolian plateau, Turkey: A record of tectonic and upper mantle processes. Earth and Planetary Science Letters 317, 85–95. doi:https://doi.org/10.1016/j.epsl.2011.12.003.

Schildgen, T.F., Yıldırım, C., Cosentino, D., Strecker, M.R., 2014. Linking slab break-off, Hellenic trench retreat, and uplift of the Central and Eastern Anatolian plateaus. Earth-Science Reviews 128, 147–168. doi:https://doi.org/10.1016/j.earscirev.2013.11.006.

Senel, M., 2002. 1:500000 scale geological maps of Turkey, No:14 Konya sheet. URL: www.mta.gov.tr.

Şengör, A., 1979. The North Anatolian transform fault: its age, offset and tectonic significance. Journal of the Geological Society 136, 269–282. doi:https://doi.org/10.1144/gsjgs.136.3.026.

Şengör, A., Yalcin, N., Canitez, N., 1980. The origin of the Adana/Cilicia Basin. An incompatibility structure arising at the common termination of the Eastern Anatolian and Dead Sea transform faults, in: Sedimentary Basins of Mediterranean Margins. C.N.R. Italian Project of Oceanography, pp. 45–46.

Şengör, A.C., 1976. Collision of irregular continental margins: Implications for foreland deformation of Alpine-type orogens. Geology 4, 779–782. doi:https://doi.org/10.1130/0091-7613(1976)4<779:COICMI>2.0.CO;2.

Şengör, A.C., Zabcı, C., Natal'in, B.A., 2019a. Continental transform faults: congruence and incongruence with normal plate kinematics, in: Transform plate boundaries and fracture zones. Elsevier, pp. 169–247. doi:https://doi.org/10.1016/B978-0-12-812064-4.00009-8.

Şengör, A.M.C., Görür, N., Şaroğlu, F., 1985. Strike-Slip Faulting and Related Basin Formation in Zones of Tectonic Escape: Turkey as a Case Study1, in: Biddle, K.T., Christie-Blick, N. (Eds.), Strike-Slip Deformation, Basin Formation, and Sedimentation. SEPM Society for Sedimentary Geology. volume 37, p. 0. doi:https://doi.org/10.2110/pec.85.37.0211.

Şengör, A.M.C., Lom, N., Sunal, G., Zabci, C., Sancar, T., 2019b. The phanerozoic paleotectonics of Turkey. Part I: an inventory. Mediterranean Geoscience Reviews 1, 91–161. doi:https://doi.org/10.1007/s42990-019-00007-3.

Şengör, A.M.C., Zabci, C., 2019. The North Anatolian Fault and the North Anatolian Shear Zone BT , in: Kuzucuoglu, C., Çiner, A., Kazanci, N. (Eds.), Landscapes and Landforms of Turkey. Springer International Publishing, Cham, pp. 481–494. doi:https://doi.org/10.1007/978-3-030-03515-0-27.

Serpelloni, E., Cavaliere, A., Martelli, L., Pintori, F., Anderlini, L., Borghi, A., Randazzo, D., Bruni, S., Devoti, R., Perfetti, P., Cacciaguerra, S., 2022. Surface Velocities and Strain-Rates in the Euro-Mediterranean Region From Massive GPS Data Processing. Frontiers in Earth Science 10, 1–21. doi:https://doi.org/10.3389/feart.2022.907897.

Serpelloni, E., Vannucci, G., Anderlini, L., Bennett, R., 2016. Kinematics, seismotectonics and seismic potential of the eastern sector of the European Alps from GPS and seismic deformation data. Tectonophysics 688, 157–181. doi:https://doi.org/10.1016/j.tecto.2016.09.026.

Sternai, P., Sue, C., Husson, L., Serpelloni, E., Becker, T.W., Willett, S.D., Faccenna, C., Di Giulio, A., Spada, G., Jolivet, L., Valla, P., Petit, C., Nocquet, J.M., Walpersdorf, A., Castelltort, S., 2019. Present-day uplift of the European Alps: Evaluating mechanisms and models of their relative contributions. Earth-Science Reviews 190, 589–604. doi:https://doi.org/10.1016/j.earscirev.2019.01.005.

Toda, S., Stein, R., Özbakir, A., Gonzalez-Huizar, H., Sevilgen, V., Lotto, G., Sevilgen, S., 2023. Stress change calculations provide clues to aftershocks in 2023 Türkiye earthquakes, Temblor.

Ulu, U., 2002. 1:500000 scale geological maps of Turkey, No: 15 Adana sheet. URL: www.mta.gov.tr.

Umhoefer, P.J., Thomson, S.N., Lefebvre, C., Cosca, M.A., Teyssier, C., Whitney, D.L., 2020. Cenozoic tectonic evolution of the Ecemiş fault zone and adjacent basins, central Anatolia, Turkey, during the transition from

Arabia-Eurasia collision to escape tectonics. Geosphere 16, 1358–1384. doi:https://doi.org/10.1130/GES02255.1.

Viltres, R., Jónsson, S., Alothman, A.O., Liu, S., Leroy, S., Masson, F., Doubre, C., Reilinger, R., 2022. Present-Day Motion of the Arabian Plate. Tectonics 41, e2021TC007013. doi:https://doi.org/10.1029/2021TC007013.

Walpersdorf, A., Pinget, L., Vernant, P., Sue, C., Deprez, A., the RENAG team, 2018. Does Long-Term GPS in the Western Alps Finally Confirm Earthquake Mechanisms? Tectonics 37, 3721–3737. doi:https://doi.org/10.1029/2018TC005054.

Walters, R.J., Parsons, B., Wright, T.J., 2014. Constraining crustal velocity fields with InSAR for Eastern Turkey: Limits to the block-like behavior of Eastern Anatolia. Journal of Geophysical Research: Solid Earth 119, 5215–5234. doi:https://doi.org/10.1002/2013JB010909.

Wang, K., Wells, R., Mazzotti, S., Hyndman, R.D., Sagiya, T., 2003. A revised dislocation model of interseismic deformation of the Cascadia subduction zone. Journal of Geophysical Research: Solid Earth 108. doi:https://doi.org/10.1029/2001JB001227.

Weiss, J.R., Walters, R.J., Morishita, Y., Wright, T.J., Lazecky, M., Wang, H., Hussain, E., Hooper, A.J., Elliott, J.R., Rollins, C., Yu, C., González, P.J., Spaans, K., Li, Z., Parsons, B., 2020. High-Resolution Surface Velocities and Strain for Anatolia From Sentinel-1 InSAR and GNSS Data. Geophysical Research Letters 47, e2020GL087376. doi:https://doi.org/10.1029/2020GL087376.

Welford, J.K., Hall, J., Rahimi, A., Reiche, S., Hübscher, C., Louden, K., 2015. Crustal structure from the Hecataeus Rise to the Levantine Basin, eastern Mediterranean, from seismic refraction and gravity modelling. Geophysical Journal International 203, 2055–2069. doi:https://doi.org/10.1093/gji/ggv422.

Westaway, R., 2003. Kinematics of the Middle East and eastern Mediterranean updated. Turkish Journal of Earth Sciences 12, 5–46. doi:https://doi.org/10.3906/yer-0301-1.

Williams, G.D., Ünlügenç, U.C., Kelling, G., Demirkol, C., 1995. Tectonic controls on stratigraphic evolution of the Adana Basin, Turkey. Journal of the Geological Society 152, 873–882. doi:https://doi.org/10.1144/gsjgs.152.5.0873.

Yıldırım, C., Sarıkaya, M.A., Çiner, A., 2016. Late Pleistocene intraplate extension of the Central Anatolian Plateau, Turkey: Inferences from cosmogenic exposure dating of alluvial fan, landslide, and moraine surfaces along the Ecemiş Fault Zone. Tectonics 35, 1446–1464. doi:https://doi.org/10.1002/2015TC004038.

Zhao, L., Paul, A., Malusà, M.G., Xu, X., Zheng, T., Solarino, S., Guillot, S., Schwartz, S., Dumont, T., Salimbeni, S., Aubert, C., Pondrelli, S., Wang, Q., Zhu, R., 2016. Continuity of the Alpine slab unraveled by high-resolution P wave tomography. Journal of Geophysical Research: Solid Earth 121, 8720–8737. doi:https://doi.org/10.1002/2016JB013310.

Özkan, A., Yavaşoğlu, H.H., Masson, F., 2023. Present-day strain accumulations and fault kinematics at the Hatay Triple Junction using new geodetic constraints. Tectonophysics 854, 229819. doi:https://doi.org/10.1016/j.tecto.2023.229819.

Figure Captions

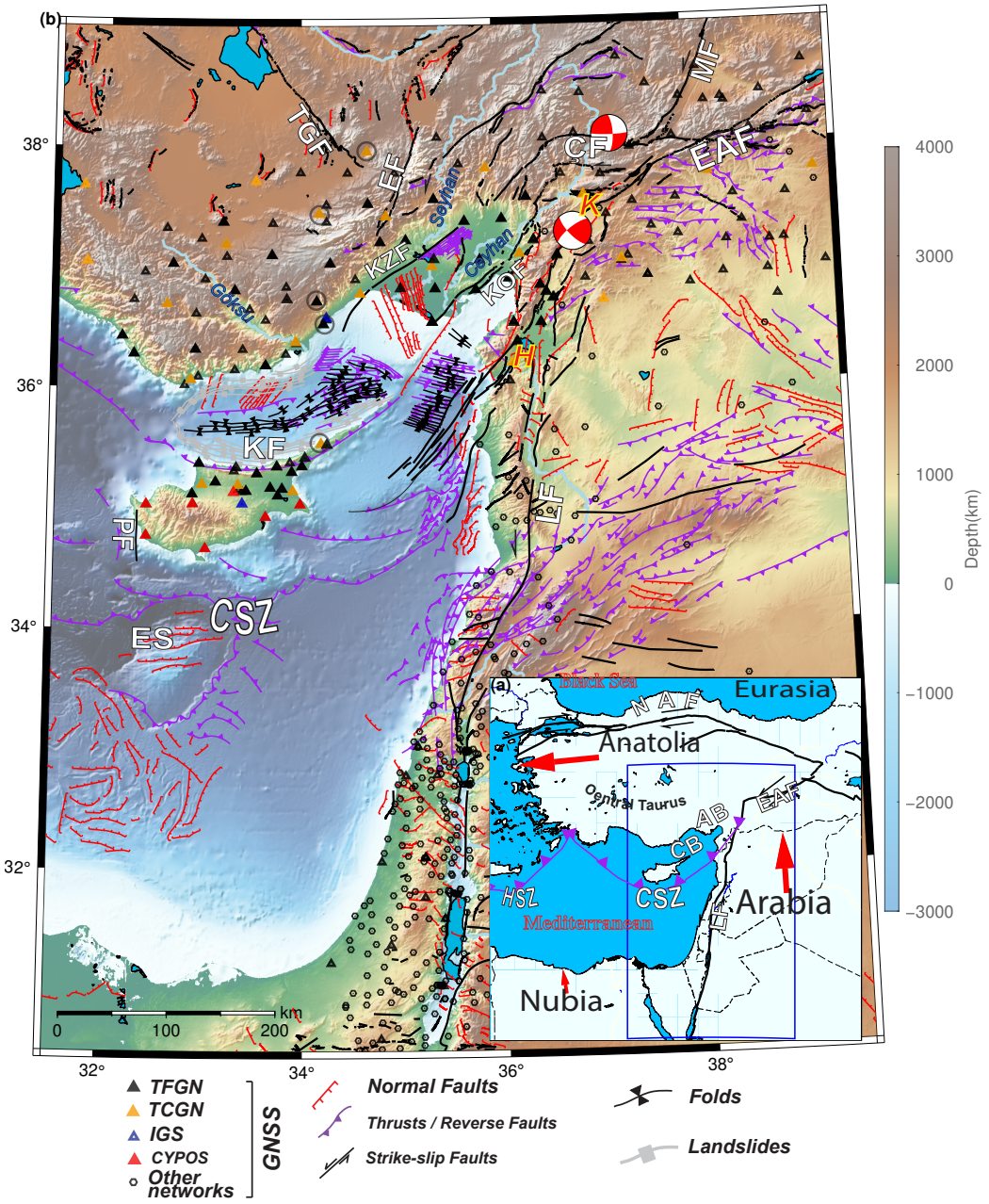

Figure 1: a) Tectonics of the Eastern Mediterranean and fundamental features in the scope of this study. Abbreviations: EAF: East Anatolian Fault, NAF: North Anatolian Fault, LF: Levant Fault, CSZ: Cyprus Subduction Zone, HSZ: Hellenic Subduction Zone, AB: Adana Basin, CB: Cilicia Basin b) Tectonic structures and GNSS sites around the region. Structures digitized from Emre et al. (2013, 2018); Şengör and Zabci (2019), the structures around Adana/Cilicia basins are taken from Aksu et al. (2005); Burton-Ferguson et al. (2005); Aksu et al. (2014a, 2021, and cited studies therein). The stations enclosed within ellipses correspond to the sites discussed in the uplift context outlined in section 4.4. Focal mechanisms belong to 06 Feb 2023 Mw=7.8 and Mw=7.6 Kahramanmaraş Pazarcık and Elbistan earthquakes. Abbreviations: K=Kahramanmaraş triple junction, H=Hatay triple junction, KF: Kyrenia Fault, ÇF: Çardak Fault, MF: Malatya Fault, EF: Ecemiş Fault, KOF: Karataş-Osmaniye Fault, TGF: Tuz Gölü Fault, KZF: Kozan Fault, PF: Paphos Fault, ES: Eratosthenes Seamount, IGS: International GNSS Service, TCGN: Turkey Continuous GNSS Network, TFGN: Turkey Fundamental GNSS Network, CYPOS:

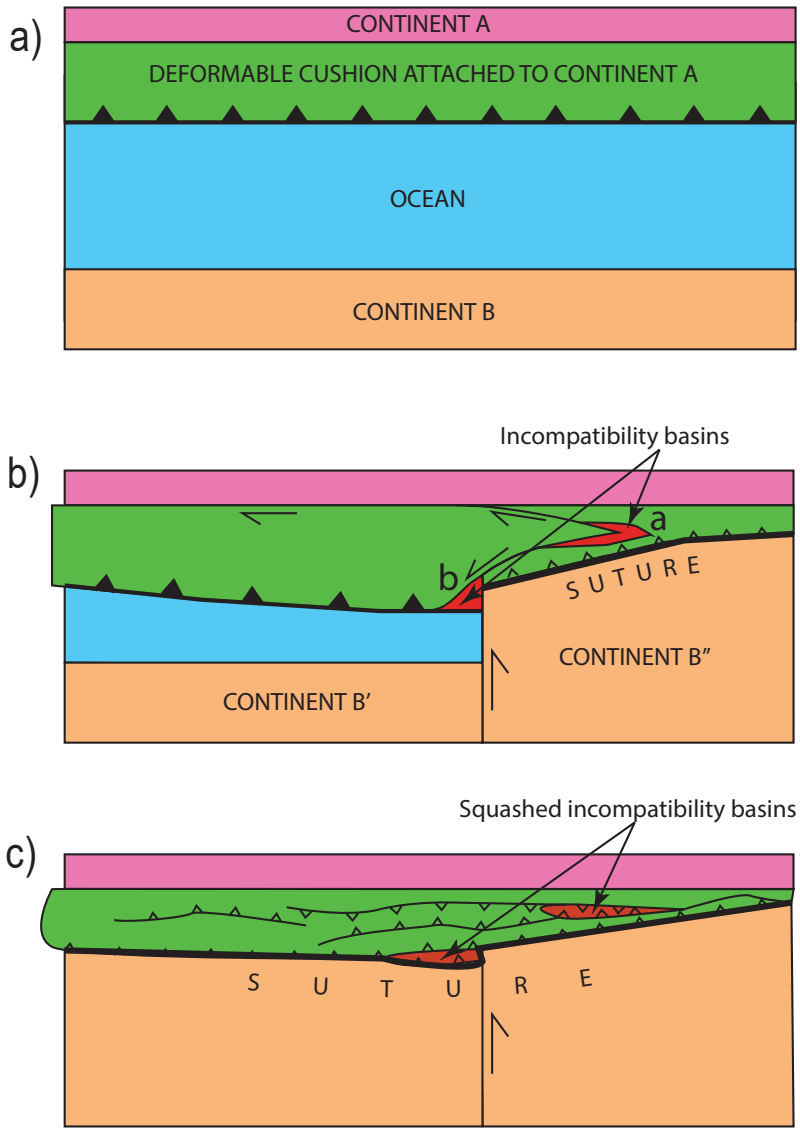

Figure 2: A sketch in map view depicts incompatibility basins arising from triple junctions and their fate: a) Continent A and continent B are approaching at the expense of the intervening ocean, which is being consumed beneath continent A creating an easily deformable cushion at its margin. b) Continent B is divided into two pieces, B' and B" by a north-south striking transform fault. When continent B" collides with continent A's easily deformable cushion, it creates two strike-slip faults along which a portion of the easily deformable part of A is expelled westward. This leads to the formation of a Karlıova-type incompatibility basin at a, and an Adana/Cilicia-type incompatibilty basin at b. c) When full collision occurs following the elimination of all ocean between the two approaching continents, the previously formed incompatibility basins will also be squashed and obliterated out of recognition, except by careful local geological studies.

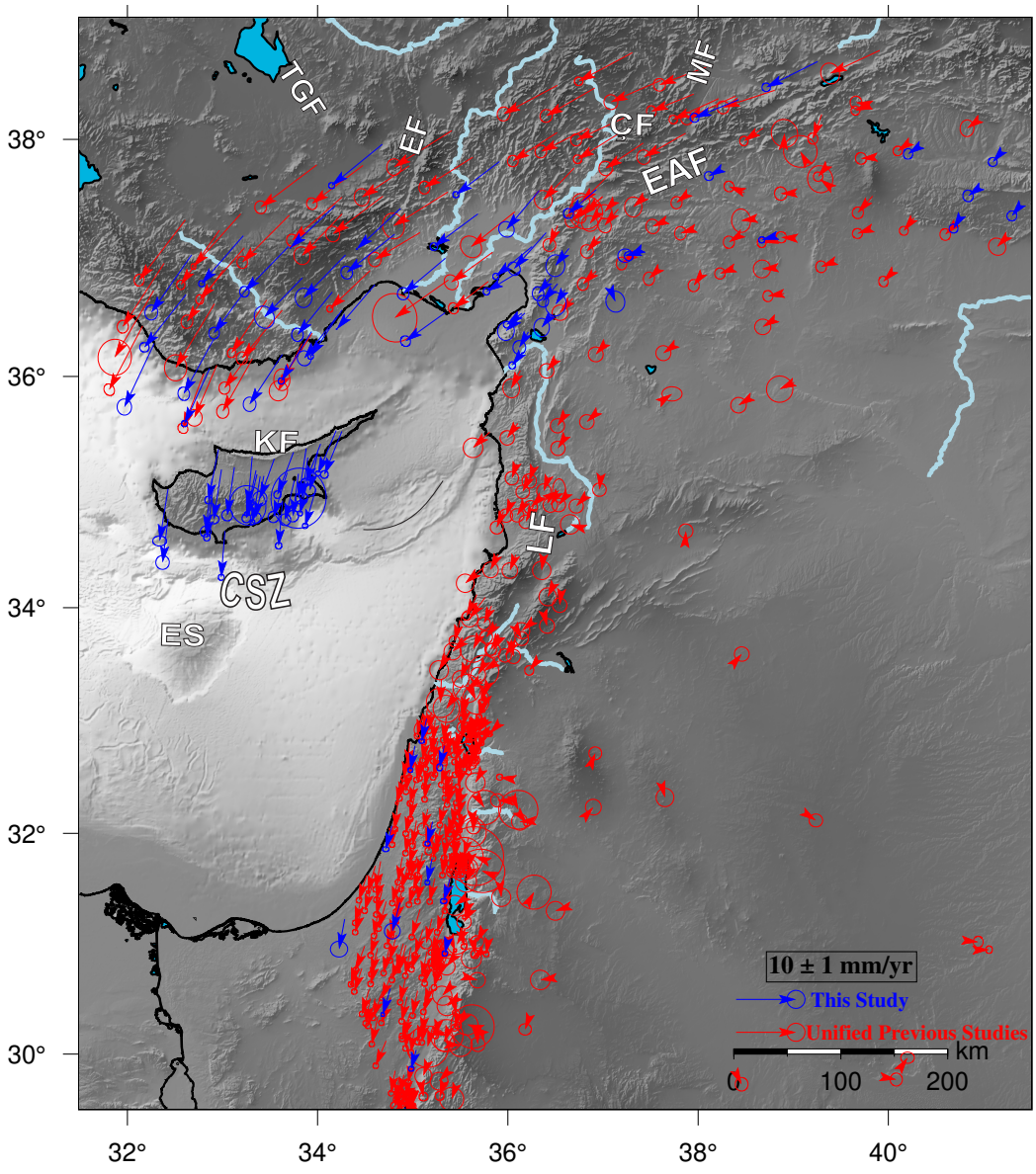

Figure 3: Unified GNSS velocity field with respect to the Arabian fixed reference frame. Blue arrows represent the newly derived rates and red arrows show previous studies previously-published rates.

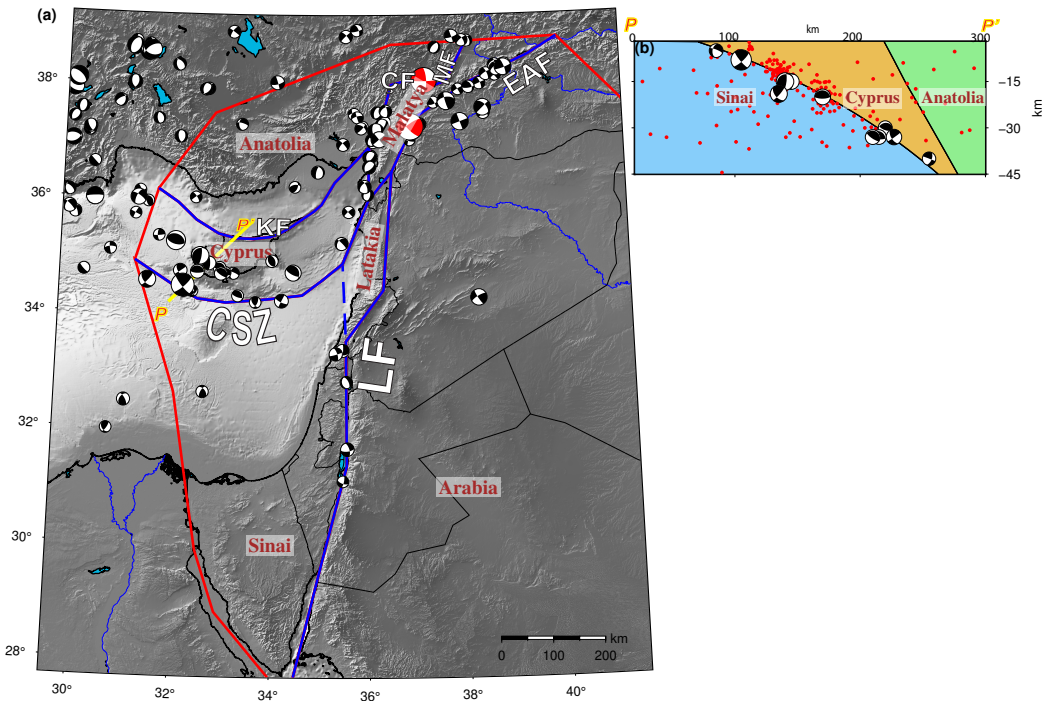

Figure 4: a) Block geometry and seismic activity around the region. Blue lines represent the boundaries defined as dislocation sources, red lines correspond to the other block boundaries which do not accumulate elastic strain. Focal mechanisms represent the earthquakes $Mw >= 4.5$ between 1976-2022 (Ekström and Nettles, 1997) (the Feb 6 2023 earthquakes are highlighted in red). They were scaled according to their magnitudes. b) The cross sectional view (marked as P-P' in the map) from the northern tip of the Cyprus Arc to the Kyrenia range (∼35 km width). Focal mechanisms (Ekström and Nettles, 1997) and red dots (KOERI, 2001; http://www.koeri.boun.edu.tr), which are the earthquakes coincide with the domain of the cross section, were projected onto the section.

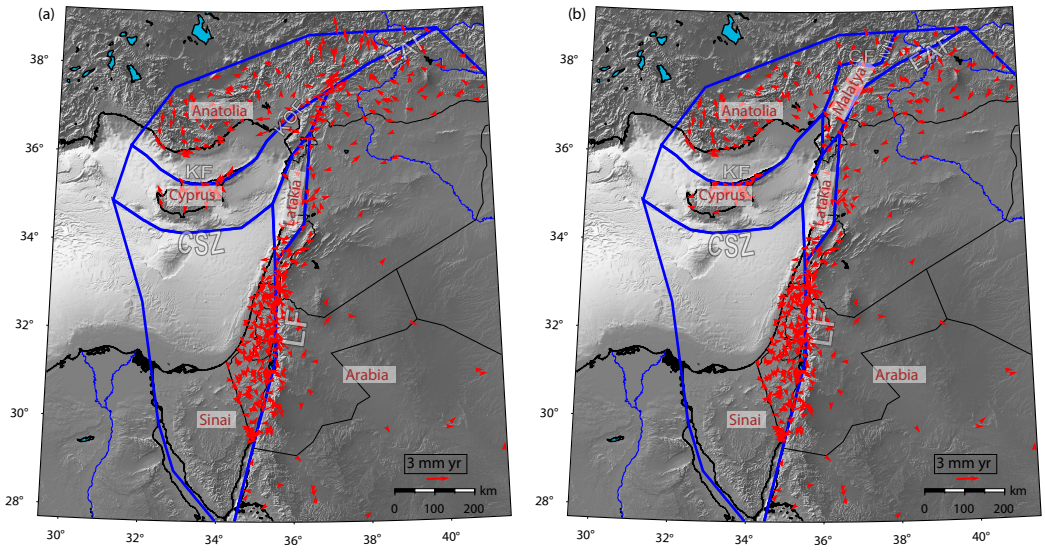

Figure 5: Comparing Diverse Block Geometries: a) This model adheres to the fault geometries proposed by Özkan et al. (2023) for Anatolia, without considering the Malatya block. b) Implementing the geometry as depicted in Fig.4a. The red arrows signify the residual velocities for each respective model.

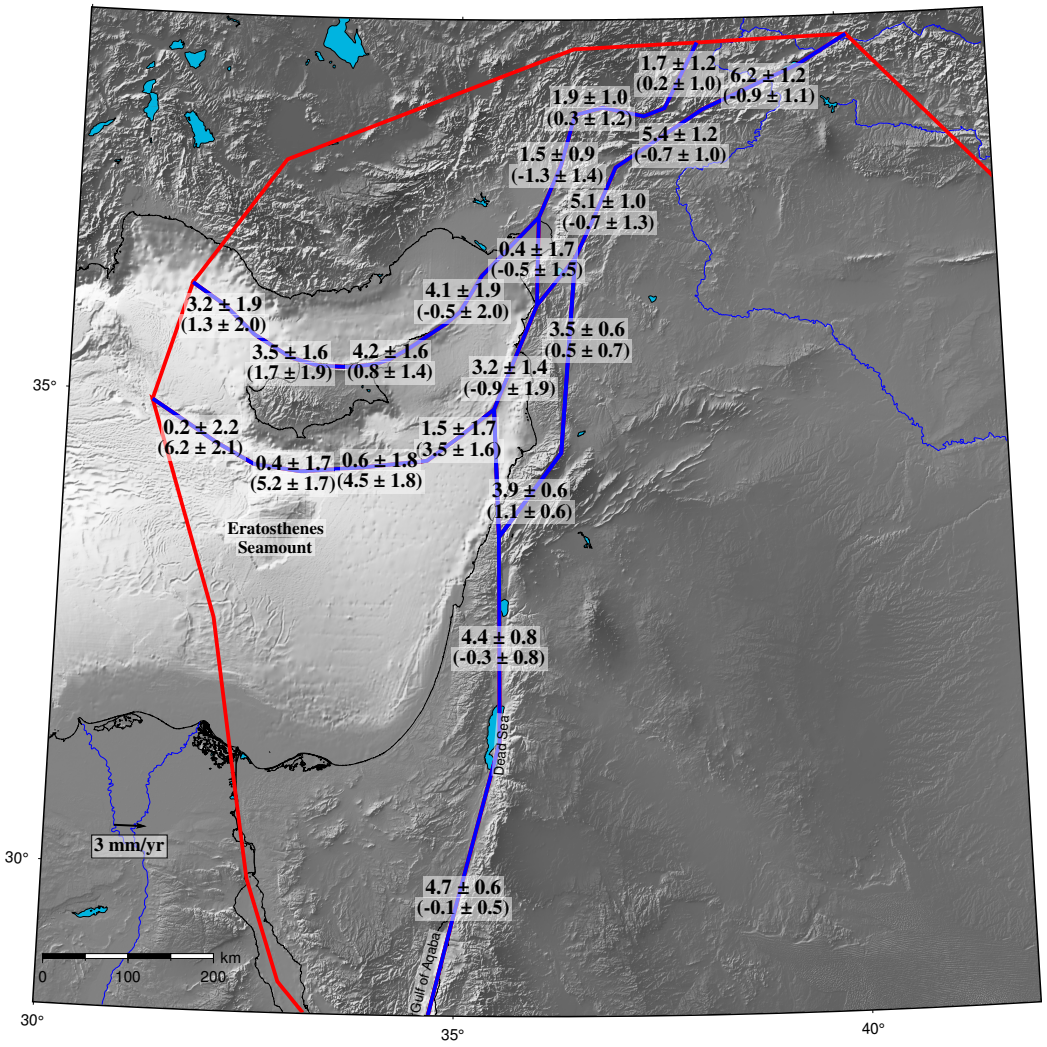

Figure 6: a) Modeled fault slip rates and residual velocities. The values with no parentheses are the strike-slip rates (Positive means left lateral) and the slip rates within the parentheses are convergence rates (positive means compression). Red arrows are the strain rate crosses for each block.

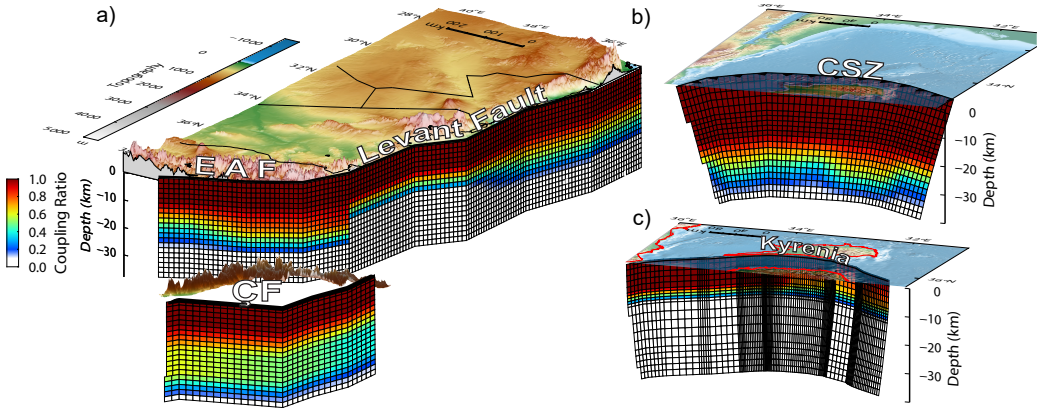

Figure 7: The distribution of locking on the dislocation sources within the block model. a) Levant, East Anatolian, and Çardak Faults (and the prolongation of the northwestern boundary of the Malatya block), b) Cyprus Subduction Zone, and c) Kyrenia fault.

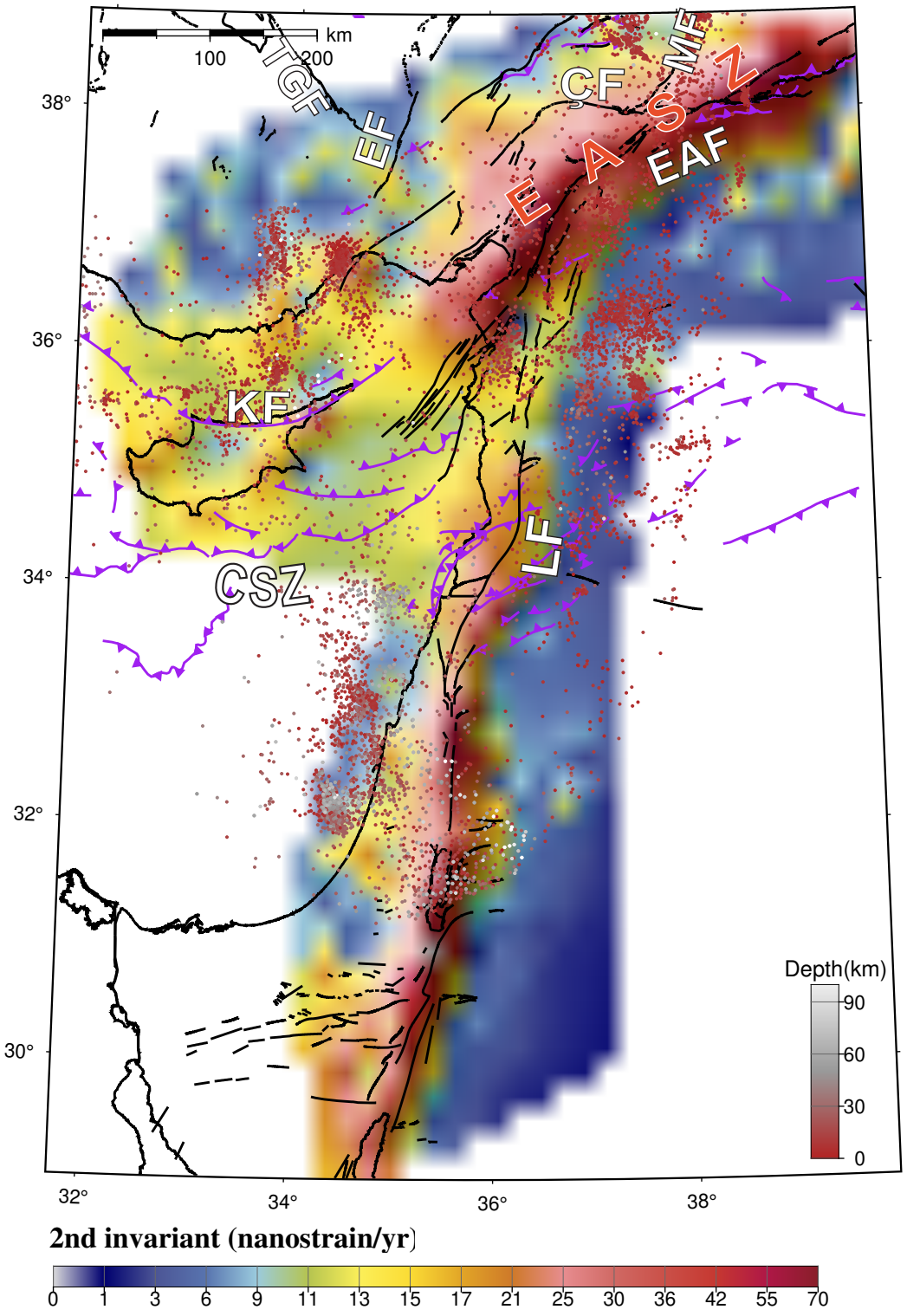

Figure 8: Seismicity, color-coded by depth, and the second invariant of the strain rate tensor. Seismicity catalog was taken from (KOERI, 2001; http://www.koeri.boun.edu.tr). EASZ: East Anatolian Shear Zone

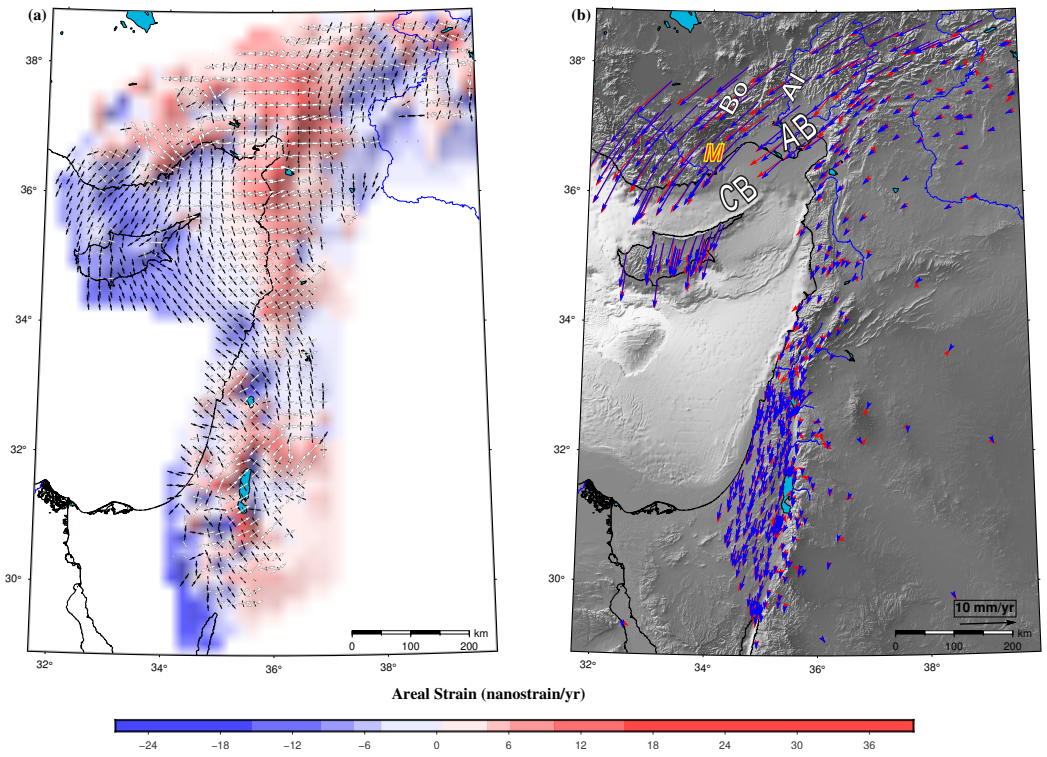

Figure 9: a) Strain rate field of the area. Arrow crosses are the principal strain rate tensor components. Black arrow belongs to the compression component of each tensor while white ones are the extensional component. Magnitudes of the principal rate crosses were normalized. The grid represents the areal strain change that accounts for the trace of the tensor for each cell (Blue means that the dominant force of the cell is compression, while red implies extension). b) Observed (red) and predicted (blue) GNSS velocities. Bo: Bolkardağ, Al: Aladağlar.

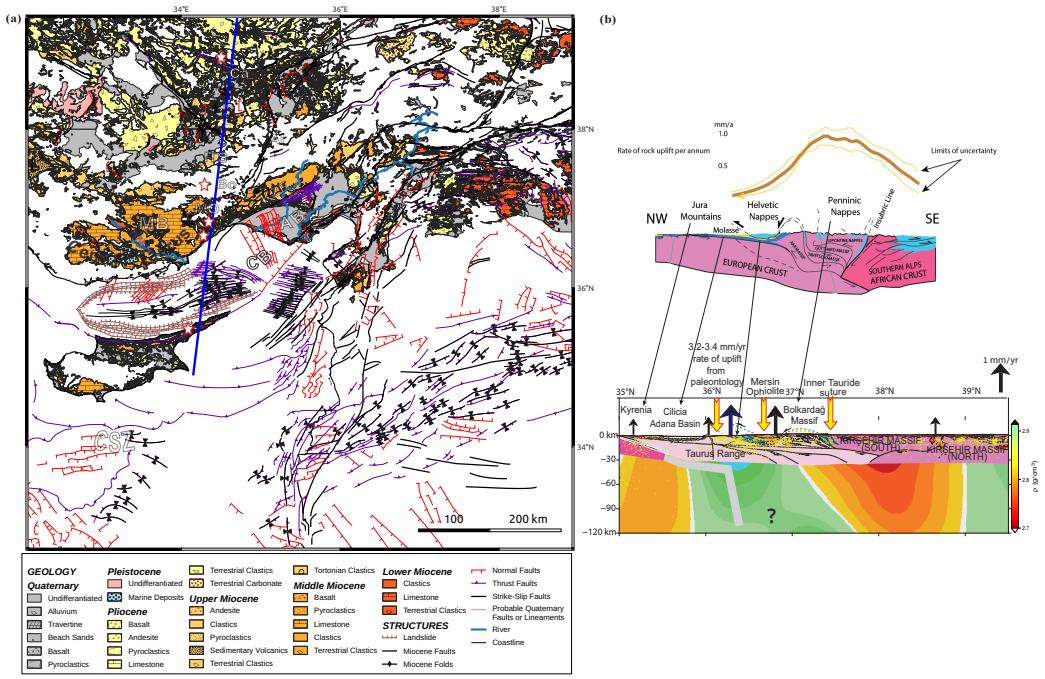

Figure 10: a) Tectonic formations and structures younger than Oligocene. Geologic formations, digitized from (Ed. Senel, 2002, Geological Map of Turkey, Adana), (Ed. Ulu, 2002, Geological Map of Turkey, Konya), and some formations were updated according to Öğretmen et al. (2018, fig. 2). Tectonic structures were compiled from Emre et al. (2013, 2018); Şengör and Zabci (2019); Aksu et al. (2005); Burton-Ferguson et al. (2005); Aksu et al. (2014a, 2021, and cited studies therein). The solid blue line corresponds to the location of the cross-section displayed in panel (b). GNSS stations are showed as white stars. MB: Mut Basin, Bo: Bolkardağ, Al: Aladağlar, ITS: Inner Tauride Suture, MO: Mersin Ophiolite, Ca: Cappadocia. b) A cross-section from the southeast of Cyprus to Central Anatolia, with a comparative analysis involving the Alps. The upper portion comprises geological interpretations extracted from (Şengör et al., 2019b), while the lower part displays a density model derived from tomography (Karabulut et al., 2019). Black arrows indicate the GNSS uplift rates from stations labeled with stars in panel a). The analogy suggests that the Kyrenia Range corresponds to the Jura Mountains, and the Adana/Cilicia Basin serves as an equivalent to the Alpine molasse basin, with the Taurus Range and Bolkardağ Massif resembling the Helvetic Nappes and Lepontine Nappes, respectively. Long-term seismicity data were projected onto the section (KOERI, 2001; http://www.koeri.boun.edu.tr), and the tomography aligns with the 34°N generated from Karabulut et al. (2019).